Annual Progress Report and Quarterly Report
for the period
April 1, 1992 through August 31, 1992

for

United States Department of Commerce
Grant No. 60NANBOD1035

"Fundamental Mechanisms for CO and Soot Formation in Diffusion Flames"

by
Robert J. Santoro
The Pennsylvania State University
Department of Mechanical Engineering
University Park, PA 16802

March, 1993

1.0   Introduction

The following report summarized the progress achieved during the period April 1, 1992

through August 30, 1992 for grant 60NANBOD1035, "Fundamental Mechanisms for CO and Soot

Formation in Diffusion Flames." This report will also serve as an annual report for the program.

The report will summarize the results obtained of the effects of soot concentration on the production

of carbon monoxide in overventilated laminar diffusion flames and will describe recent results on

underventilated diffusion flames. The former studies were conducted in collaboration with Dr.

Kermit Smyth of NIST, while the latter studies were conducted in collaboration with Dr. George

Mulholland of NIST during his sabbatical leave at Penn State last year.

2.0   Accomplishments

2.1 The Oxidation of Carbon Monoxide and Soot in Hydrocarbon Diffusion Flames

One of the major objectives of the current research program is to examine the effect of the

presence of soot particles on carbon monoxide (CO) production in laminar diffusion flames. The

basis for arguing that soot affects the CO concentration levels in diffusion flames is based on two

concepts. First, soot particles radiate strongly and, thus, can lower the temperature in the flame

significantly slowing the chemical reactions which result in the oxidation of CO. Secondly, soot itself

can be oxidized in the flame mainly through reactions with hydroxyl radicals (OH). Since the

primary step in the oxidation of CO also involves OH in the temperature range of interest, soot

oxidation represents a competitive pathway for the removal of OH. If the reactivity of the soot

particles is large enough, soot could impede CO oxidation as well as add CO species as a result of its

oxidation.

In order to vary the soot concentration systematically, a fuel mixture approach has been

utilized in which methane, methane/butane and methane/butene flames have been studied. This

approach allows the soot concentration to be varied significantly while holding the flame size and

shape nearly constant. Carbon monoxide measurements have been obtained along the center line of

the flame using a sampling probe approach followed by gas chromatographic analysis. Laser-induced fluorescence measurements carried out in collaboration with Dr. Kermit Smyth of NIST have been employed to determine the OH concentrations throughout the flame. Previous publications have described the CO measurements and the OH measurement approach [1,2]. Recently, a full description of the current results has been submitted to *Combustion and Flame* for publication [3] and is included as Appendix A. Consequently, only a brief summary of the present results will be given, and the reader is referred to Appendix A for details.

Quantitative OH concentrations and primary soot particle sizes have been determined in the soot oxidation regions of axisymmetric diffusion flames burning methane, methane/butane, and methane/1-butene in air at atmospheric pressure. The total carbon flow rate was held constant in these flames while the amount of soot was varied considerably. Laser-induced fluorescence measurements of OH were placed on an absolute basis by calibration against earlier absorption results. The primary size measurements of the soot particles were made using thermophoretic sampling and transmission electron microscopy.

OH concentrations are greatly reduced in the presence of soot particles. Whereas large super-equilibrium ratios are observed in the high-temperature reaction zones in the absence of soot, the OH concentrations approach equilibrium values when the soot loading is high. The diminished OH concentrations are found to arise from reactions with the soot particles and only to a minor degree from lower temperatures due to soot radiation losses. Analysis of the soot oxidation rates computed from the primary particle size profiles as a function of time along the flame center lines show that OH is the dominant oxidizer of soot, with O_2 making only a small contribution. Higher collision efficiencies of OH reactions with soot particles are found for the flames containing larger soot concentrations at lower temperatures. A comparison of the soot and CO oxidation rates shows that

although CO is inherently more reactive than soot, the soot successfully competes with CO for OH and hence suppresses CO oxidation for large soot concentrations.

2.2 Generation of CO and Smoke During Underventilated Combustion

In order to further study the generation of CO and its relationship to soot formed in fires, a series of studies of underventilated flame have been undertaken. This particular flame configuration has not been widely studied and little is known about the behavior of CO and soot for underventilated conditions in laminar flames.

To address this problem, a new burner facility was developed specifically to study laminar diffusion flames for underventilated conditions. For the initial studies, measurements of CO and soot yields as a function of the global or overall equivalence ratio were desired. Consequently, the burner was designed to accommodate probe sampling measurements at the exit of the burner chimney. A nitrogen dilution system was incorporated into the burner to quench and rapidly mix the flame combustion products prior to sampling. This process allowed for single point measurements of the CO and soot concentrations which would be representative of the overall production of these species in these underventilated flames.

The CO and smoke yields observed for underventilated laminar diffusion flames were determined for methane and ethene fuels for global equivalence of Φ over the range 0.5 to 4.0. The peak CO yields for methane and ethene, 0.37 and 0.47 respectively, are at least a factor of 100 greater than for overventilated burning. The ratio of CO/CO_2 versus Φ for the methane flame have also been compared with local measurements of this ratio for both overventilated and underventilated laminar diffusion flames and with the results for turbulent nature gas flames quenched in an upper layer. The peak smoke yields for methane and ethene are 0.01 and 0.05, respectively, compared to yields of 0 and 0.028 for the overventilated case. The proportionality between smoke yield and CO yield observed for overventilated burning for a wide range of fuels is found not to be valid for the underventilated case. The chemical makeup and structure of the smoke produced at high equivalence

ratio is qualitatively different from smoke produced under overventilated conditions; the smoke is mainly organic rather than graphitic and it has an agglutinated structure rather than an agglomerate structure with distinct primary spheres usually observed in overventilated burning.

Further details on the results are contained in Appendix B, which contains a paper in preparation for submission to *Combustion and Flame*.

3.0 Summary

The results of the studies conducted over the past year have clearly established the relationship between soot concentration and CO under overventilated conditions for laminar diffusion flames. The effects of the presence of soot particles on CO production occurs through a reduction in the OH radical concentrations in the flame. Although radiative effects are also important, the competition for OH by soot particles is the major reason for the reduction in the CO oxidation as soot particle concentration increases.

The second major accomplishment during the past year involves our investigations of underventilated laminar diffusion flames. These flames show much higher concentrations of CO as compared to overventilated flames. The studies to date have been examining the overall or global behavior of these flames as a function of equivalence ratio. Clearly, more detailed measurements within the flame are required and represent a current thrust of the program over the next year. Nonetheless, the concentration levels observed are comparable to those observed in actual room fine situations. Thus, these simple flames may provide an excellent environment in which to examine the mechanism of CO production which is representative of some real fire situations. Furthermore, the tractable fluid mechanic environment provided by laminar flames may provide a useful modeling test case for numerical codes intended to represent the production of CO in fires.

References

1. Puri, R. and Santoro, R. J., Fire Safety Science-Proceedings of the Third International Symposium, p. 595 (1991).

2. Puri, R., Moser, M., Santoro, R. J. and Smyth, K. C., Twenty-Fourth Symposium (International) on Combustion, The Combustion Institute, p. 1015 (1992).

3. Puri, R., Santoro, R. J. and Smyth, K. C., "The Oxidation of Carbon Monoxide and Soot in Hydrocarbon Diffusion Flames," submitted to *Combustion and Flame*.

THE OXIDATION OF CARBON MONOXIDE AND SOOT

IN HYDROCARBON DIFFUSION FLAMES

Rahul Puri and Robert J. Santoro

Department of Mechanical Engineering
The Pennsylvania State University
University Park, PA 16802

and

Kermit C. Smyth

Building and Fire Research Laboratory
National Institute of Standards and Technology
Gaithersburg, MD 20899

ABSTRACT

Quantitative OH· concentrations and primary soot particle sizes have been determined in the soot oxidation regions of axisymmetric diffusion flames burning methane, methane/butane, and methane/1-butene in air at atmospheric pressure. The total carbon flow rate was held constant in these flames while the amount of soot was varied considerably. Laser-induced fluorescence measurements of OH· were placed on an absolute basis by calibration against earlier absorption results. The primary size measurements of the soot particles were made using thermophoretic sampling and transmission electron microscopy.

OH· concentrations are greatly reduced in the presence of soot particles. Whereas large super-equilibrium ratios are observed in the high-temperature reaction zones in the absence of soot, the OH· concentrations approach equilibrium values when the soot loading is high. The diminished OH· concentrations are found to arise from reactions with the soot particles and only to a minor degree from lower temperatures due to soot radiation losses. Analysis of the soot oxidation rates computed from the primary particle size profiles as a function of time along the flame centerlines show that OH· is the dominant oxidizer of soot, with O_2 making only a small contribution. Higher collision efficiencies of OH· reactions with soot particles are found for the flames containing larger soot concentrations at lower temperatures. A comparison of the soot and CO oxidation rates shows that although CO is inherently more reactive than soot, the soot successfully competes with CO for OH· and hence suppresses CO oxidation for large soot concentrations.

I. INTRODUCTION

In recent years increasing attention has been devoted to oxidation processes in hydrocarbon diffusion flames due to their key role in the production of combustion generated pollutants. Not only does the soot oxidation step determine the amount of smoke that will be emitted from a flame, but it also strongly influences the quantity of carbon monoxide (CO) that will survive a given combustion process [1]. Emissions of both CO and soot particles present significant fire hazards, indicate poor combustion efficiency, and are objectionable from an environmental standpoint.

Prior to the work of Fenimore and Jones [2] that elucidated the importance of OH· radicals, soot oxidation rates were calculated using the expression determined by Nagle and Strickland-Constable (NSC) for pyrographite oxidation [3] by assuming that molecular oxygen alone was responsible. Neoh et al. [4] also showed that OH· is the primary oxidant of soot in the main reaction zone of premixed flames and that the contribution of molecular oxygen is significant only when the oxygen mole fraction is greater than 5%. The recent study of Dixon-Lewis et al. [5] has reopened the question of whether OH· or O_2 is the primary oxidant of soot in the main reaction zone of premixed flames. They proposed a catalytic mechanism in which H atoms react with O_2 at or close to

the soot surface to produce either OH· radicals or O atoms which then more efficiently attack soot.

Soot oxidation studies have often assumed that soot particles are spherical and have used laser light scattering and extinction measurements to obtain information on their size [6]. In reality the soot particles are agglomerates of a variable number of smaller, uniformly sized, more or less spherical "primary" particles [7]. Therefore, the assumption of spherical particles can result in a significant error in the estimation of the particle surface area and thus the oxidation rate. With the incorporation of fractal concepts, it is now possible to obtain a reasonable estimate of the surface area of agglomerated soot particles [8].

Despite these advances in characterizing the soot particle surface area, complexities exist in determining the fraction of the surface area that participates in reactions, i.e. the number of active sites. Although the concept of reactions at active sites is relatively new in the area of soot surface growth, it was proposed over 40 years ago to explain the heterogeneous reactions of various gases with carbon [9]. In fact the NSC expression is based on a concept similar to the active sites approach. Howard [10] has recently suggested an active site description involving radicals for soot oxidation by OH· . His re-evaluation of previous data [4] showed an interesting correlation between the H/C ratio in the soot and the measured collision efficiency of soot with OH· .

Not much is known about the nature and origin of active sites for either soot growth or oxidation processes. Tesner [11] argues that active sites are formed when reactive species collide with the incipient particle surface. Once formed, these sites are thought to be self-renewing [12] and are not affected by coagulation, surface growth, or gas phase chemistry [13]. It is not known whether the same active sites that participate in the surface growth reactions following soot inception also play a role in oxidation processes. Recent X-ray photoelectron spectroscopy investigations of soot particles [14,15] have shown adsorbed as well as chemically bound oxygen to be present on soot particles. It has been suggested [15] that the active sites include surface-adsorbed oxygenated complexes which are responsible for the catalytic reactivity of the carbon particles.

Our understanding of soot oxidation in terms of both the reactive area as well as the primary oxidant is still not complete. In the present investigation concentration profiles of the hydroxyl radical have been obtained in the soot oxidation regions of laminar, hydrocarbon diffusion flames using laser-induced fluorescence. The data have been placed on a quantitative basis by calibrating [16] against an earlier absorption measurement. Soot primary particle size measurements were also made using a thermophoretic sampling procedure [7] followed by Transmission Electron Microscopy (TEM). The time evolution of the primary particle profiles have been used in conjunction with results of a

fractal aggregate analysis to calculate soot oxidation rates. Specific attention is devoted here to the factors which control the OH· concentrations in the soot oxidation region.

II. EXPERIMENTAL APPROACH

A coannular burner consisting of a 1.1 cm diameter fuel tube and a concentric 10.2 cm diameter air annulus [17] was used to establish the laminar diffusion flames. CP grade purity (99%) fuels were used in these studies, while an in-house compressor was employed to supply the air. The air and fuel flows to the burners were metered with rotameters, which were arranged to allow mixing of two fuels. A fuel mixture approach was adopted in order to vary the soot concentration while keeping the total carbon flow rate constant, which ensured similar flame sizes and shapes. Flames burning methane (9.8 cm^3/s) and methane (5.6 cm^3/s) doped with either butane (1.05 cm^3/s) or 1-butene (1.05 cm^3/s) were studied. The air flow rate was maintained at 1300 cm^3/s for all flames.

A. OH· Concentration Measurement

Figure 1 presents a schematic diagram of the laser-induced fluorescence measurement setup. The UV beam was produced by frequency doubling the output of a Nd:YAG pumped dye laser. The wavelength was tuned to 283.55 nm, which corresponds to the excitation of the $Q_1(8)$ line of the $A^2\Sigma^+ \leftarrow X^2\Pi_i$ (1,0) band of OH· .

Excitation from the $N'' = 8$ level minimizes the Boltzmann population correction with temperature (less than 5% over the temperature range 1400 to 2100 K). Since the pulse energy was high enough (~1 mJ/pulse) to easily saturate this strong transition, only the reflected beam from the first surface of a thick piece of quartz (~0.03 mJ/pulse) was passed through the flame. This procedure ensured that the laser-induced fluorescence signals were linear with the laser energy. A pyroelectric joulemeter was placed behind the quartz plate to monitor the laser energy for each pulse. The fluorescence signal was collected at 90° with a cooled CCD camera equipped with a microchannel image intensifier. Glass filters placed in front of the camera attenuated elastically scattered light from the soot particles and transmitted the (0,0) and (1,1) emission bands of OH·, as well as the broadband fluorescence which has been attributed to polycyclic aromatic hydrocarbons [18].

The details of the experimental procedure have been described elsewhere [16] and are only briefly outlined here. At each measurement location two 1-D images were obtained with the laser wavelength tuned on and off the $Q_1(8)$ excitation line of OH·. Relative intensity radial profiles were obtained from these images by binning data over several pixel rows in the region of interest. While the on-resonance profiles show signals due to OH· fluorescence, light scattered by soot particles, and PAH fluorescence, the off-resonance profiles exhibit only the latter

two contributions. Since the off-resonance images were obtained by tuning the laser wavelength by only 0.03 nm, the signals due to light scattered by soot particles and broadband PAH fluorescence were unchanged. Thus, subtracting the off-resonance profile from the on-resonance profile gives the raw OH· signal even in regions where there are significant amounts of soot.

The relative intensity of the OH· signal was calibrated using an earlier absorption measurement in a methane/air diffusion flame on a Wolfhard-Parker burner [19]. Detailed measurements of the major species have been obtained along the centerline for the axisymmetric flames studied here [1] and allow a complete quenching correction to be made [19-21]. For the radial OH· profiles only an approximate correction for the overall quenching rate (proportional to $1/\sqrt{T}$) was applied [16], since radial species profile data are not available in these flames. An additional correction must be made for determining the OH· concentrations along the centerline in order to account for the attenuation of the laser beam intensity by soot particles (absorption by OH· is less than 1% [16]). This attenuation leads to asymmetric fluorescence profiles, with the asymmetry being greatest for the methane/1-butene flame which contains the largest soot concentrations. The OH· signal profiles have been corrected using local extinction measurements of the soot particle field in identical flames [22]. Extinction values depend upon the wavelength of light being used and the refractive index of the soot particles at that wavelength. Since the latter quantity

can not be obtained with certainty, the extinction profile measurements [22] were scaled such that symmetric OH· fluorescence profiles resulted. The intensity of the laser beam could then be derived at each radial flame location.

B. Soot Primary Particle Size Measurements

A thermophoretic sampling technique similar to that used by Dobbins and Megaridis [7] was used to measure the size of the primary soot particles. The thermophoretic probe consisted of a carbon coated 200 mesh copper grid held in place between two strips of sheet metal, machined to expose the grid to the flame. The probe was rapidly inserted into the flame environment (~ 3.3 m/s) for a brief exposure duration of 50 ms before being quickly withdrawn. This exposure time is short enough to provide a cold surface to attract the soot particles as well as to quench any heterogeneous reactions on the captured particles [7]. The rapid insertion and retraction motion was made possible by mounting the probe on the displacement rod of a double acting pneumatic cylinder. The direction reversal of this cylinder was achieved by supplying the driving air (at 40 psi) through a 3-way solenoid valve controlled with a variable time-delay relay circuit.

Transmission electron microscopy (TEM) was used to examine the grids, and micrographs were obtained at a magnification of 60,000. These micrographs were then imaged with a CID camera which provided an additional, approximately ten-fold magnification. The CID

camera software was utilized to measure the primary particle size, d_p, by locating the measurement cursor at diametrically opposite sides of each primary particle and noting the coordinates. A minimum of 75 d_p measurements were made at each flame location. An image of engineering graph paper was also obtained to provide an absolute length calibration for the CID camera magnification. Finally, the primary particle sizes were obtained by accounting for the TEM magnification. The camera images had a pixel resolution varying from 0.6 nm for the methane flame images to 1 nm for the methane/1-butene flame images.

III. RESULTS

A. OH· Concentration Measurements

Figure 2 presents the OH· concentration profiles in the 9.8 cm^3/s methane/air diffusion flame at several axial locations above the fuel tube exit. The methane flame has a visible height of 10.7 cm, corresponding to the location where soot particles are completely oxidized. Therefore, the OH· concentration profiles at 10.2 and 11.4 cm correspond to locations immediately below and above the visible flame tip, respectively. It is interesting that the profile at 10.2 cm shows two OH· maxima and a valley in the region where the soot particles are being oxidized. In contrast, at this height diffusion processes result in maxima along the centerline for all fuel-derived major species (such as CO_2, CO, and

H_2O) as well as for the temperature. Once the soot particles are completely oxidized, the OH· concentration profile shows a single peak along the flame centerline at an axial position of 11.4 cm.

Figure 3 presents the OH· concentration results in the methane/butane flame. As in the methane flame the OH· profiles show evidence of OH· consumption close to the flame tip. In the methane/butane flame the profiles at 11.4 and 12.7 cm correspond to locations immediately below and above the visible flame tip at 11.7 cm. Although diffusion processes result in a single centerline peak for the temperature and the fuel-derived major species, the OH· concentration profile again exhibits two maxima at the axial location of 11.4 cm. Above the visible flame tip where there are no soot particles, the OH· profile shows a single peak along the centerline.

Figure 4 presents the OH· concentration results in the methane/1-butene flame. The methane/1-butene flame does not have a visible flame tip, since it emits smoke. In this respect the lack of buildup of OH· along the centerline of this flame suggests that reactions between OH· and soot particles strongly reduce the OH· concentrations.

B. Soot Primary Particle Size Measurements

Figure 5 presents the volume mean diameter, d_{p30}, determined from the primary particle size measurements as a function of time

along the centerline of the methane, methane/butane, and methane/1-butene flames. Also shown are the soot volume fraction measurements [22], f_v. Velocity data obtained from laser velocimetry measurements in identical flames [22] were used to convert the axial positions to time. The primary particle size in the methane and the methane/butane flames decreases rapidly and shows a convex upwards shape, consistent with particle burnout. In contrast, the methane/1-butene flame shows a concave upward shape, and the particle sizes approach a constant value. This behavior is consistent with smoking conditions.

Soot volume fraction measurements are also shown in Fig. 5 and are related to the volume mean diameter through the number concentration of the primary particles N_p:

$$f_v = \frac{\pi}{6} d_{p_{30}}{}^3 N_p. \tag{1}$$

In the present analysis N_p is assumed to be constant along the flame centerline. This assumption is based on (1) the results of a fractal aggregate analysis [8] applied to a laminar ethene/air diffusion flame along a nearly isothermal streamline passing through the location of the maximum soot volume fraction [23] and (2) the small temperature variation (less than 250 K) observed in the soot oxidation region of the flames studied here. Assuming that there is no slip between the particles and the hot combustion gases that convect the particles, a ± 125 K temperature variation at 1500 K will cause the number concentration of primary particles

to change by less than ± 10% (as determined from the temperatures
and the ideal gas law).

Data in the methane/butane flame support the relative
constancy of N_p, which has also been reported by others along
convective streamlines [24,25]. In the methane flame there are
insufficient soot volume fraction data for a similar check. For
this flame the soot volume fraction, f_v, and the d_{p30} results overlap
in time only near 0.115 s (Fig. 5). Here the shape of the profiles
suggests that both f_v and d_{p30} are close to their maximum values
along the centerline. For the methane/1-butene flame the
measurements indicate a significant increase in N_p, particularly at
earlier times. However, this may be an artifact of the
thermophoretic sampling procedure because the annular soot volume
fraction in the methane/1-butene flame is comparable to the
centerline values at the earlier times examined in the soot
oxidation region. Thus, the centerline TEM samples may have been
contaminated with soot particles from the annular region which
contains larger primary particles. Of the flames studied here such
a situation occurs in the oxidation region only for the methane/1-
butene flame. This point is important in considering the collision
efficiency of OH· with soot (see section IV.D).

IV. DISCUSSION

The OH· measurements in the methane, methane/butane, and methane/1-butene flames show that the OH· concentration is suppressed in the presence of soot particles. The larger the soot concentration, the greater the effect upon the OH· levels due to its apparent consumption in the soot oxidation region. Thus, soot particles are likely to reduce the amount of OH· available for CO oxidation. Prior investigations have also shown that the yield of CO from hydrocarbon diffusion flames is closely related to the measured soot concentrations within the flame, with larger CO concentrations surviving at the higher soot loadings [1,26]. For the flames of the present study the CO concentration measurements have been made primarily along the centerline [1]. Thus, attention will be focussed on this region.

A. Superequilibrium OH· Concentrations

Figure 6 presents the OH· concentration results along the centerline as a function of the axial position above the fuel tube exit. The error bars represent the standard error of the 22 pixel measurements that constitute the approximately constant signal about the centerline (± 1 mm). These statistical uncertainties are smaller than the symbol size for the methane and methane/butane flames where the OH· concentrations are high and the signal-to-noise levels are large. Figures 2,3,4, and 6 clearly show that as the soot concentration increases, the centerline OH· concentration

decreases. The peak centerline soot volume fractions are 0.76, 2.6 and 5.5 ppm in the methane, the methane/butane, and the methane/1-butene flames, respectively [22]. A noteworthy feature of Fig. 6 is that the OH· concentrations in the methane and the methane/butane flames reach approximately the same value along the centerline once the soot particles are completely oxidized. At an axial location of 12.7 cm the centerline temperatures (1610 K and 1549 K) and the local stoichiometries (0.84 and 0.86) are also closely similar in these two flames (see also Table I below).

The centerline and peak OH· concentration data have also been compared with equilibrium predictions [27] made using the measured temperatures and the local stoichiometries. Table I presents the results along with the flame conditions (T and ϕ) at each measurement location. With increasing height and decreasing ϕ, the superequilibrium OH· levels decrease along the centerline for all flames. It is interesting to note that in the methane/1-butene flame that emits smoke the OH· concentration along the centerline quickly approaches the equilibrium prediction at the higher measurement locations where $\phi < 1$. For axial locations where the peak OH· concentrations occur in the annular region, greater departures from the equilibrium predictions, calculated at an assumed stoichiometry of $\phi = 0.85$ [16], are observed as the soot concentration increases (see Table I). The same qualitative result has been observed for the maximum OH· concentrations measured in a

series of ethylene/air diffusion flames in which the soot volume
fraction was varied [16].

Table I shows that while the peak OH· concentration in the
methane/1-butene flame exhibits larger superequilibrium values, the
centerline OH· concentrations are closer to equilibrium values for
$\phi < 1$ than in the other flames of this study. This result can be
rationalized as follows. As the soot concentration increases in a
hydrocarbon diffusion flame, the temperatures decrease due to heat
loss by radiation. Apparently, the concentrations of the major
radicals (OH·, O:, and H·), which are controlled by fast,
bimolecular shuffle reactions and three-body recombination
reactions, do not adjust quickly to the lower temperatures. Thus,
with increasing soot concentrations and lower flame temperatures,
larger superequilibrium OH· concentrations are observed at the
location of peak OH· concentration. Note that there are no soot
particles in this region. Within the envelope of the visible flame
the lower superequilibrium ratios can be ascribed to the presence
of soot particles. The large soot surface area can serve as a sink
for the radical pool in two ways: as a reactive partner and/or as
a chaperon M for the three-body recombination reactions.

Carbon has been reported by Mulcahy and Young [28] to
efficiently catalyze the recombination reaction of OH· with H atom
at 298 K . These workers report a lower limit of 0.04 for the

collision efficiency between OH· and soot, $\eta_{OH,c}$, for the catalyzed recombination reaction:

$$H\cdot + OH\cdot + C \rightarrow H_2O + C.$$
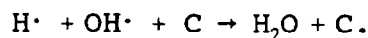
This reaction was assumed to be first order in the OH· concentration and zero order in the H-atom concentration [28]. If we assume the same value of the collision efficiency for the conditions of the present study, the normalized reaction rate of OH· ($\omega_{OH\cdot}/[OH\cdot]$) is 17,510 s^{-1} in the methane/1-butene flame at the centerline for an axial position of 8.89 cm. At the same location $\omega_{OH\cdot}/[OH\cdot]$ for the termolecular recombination reaction

$$H\cdot + OH\cdot + M \rightarrow H_2O + M$$
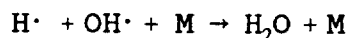
is calculated to be only 61 s^{-1}. Here the H-atom concentration was obtained from the OH· , H_2, and H_2O concentration measurements by assuming equilibration of:

$$H\cdot + H_2O \leftrightarrows OH\cdot + H_2.$$
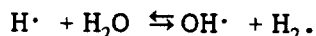
Thus, the presence of soot particles reduces the local OH· concentration and can cause a more rapid adjustment of superequilibrium OH· levels toward equilibrium values.

B. Thermal versus Chemical Effects on the OH· Concentration

Consideration will now be given to the factors that affect the OH· concentrations in these flames. Figures 2-4,6 show a strong dependence of the OH· concentration upon the local soot concentration. From equilibrium calculations one finds that the

OH· concentration depends on both the temperature and on the local stoichiometry, ϕ. It is also possible that the amount of CO, which is not uniquely related to ϕ [1], will affect the OH· concentration. Therefore, the OH· concentration can be functionally represented as follows:

$$[OH·] = f(\phi, T, [Soot], [CO]).\qquad(2)$$

The relative contributions of thermal versus chemical effects on the OH· concentration are difficult to establish in this highly coupled system. As the soot concentration increases, the temperature decreases due to radiative heat transfer. These hydrocarbon diffusion flames, therefore, do not offer the opportunity of holding one parameter fixed and varying the other parameters. However, estimates of thermal versus chemical effects can still be made. Equilibrium predictions of the OH· concentration show a weak dependence on ϕ in the fuel lean region ($\phi \leq 0.95$). Therefore, Eq. 1 can be rewritten as

$$[OH·] = f(T, [Soot], [CO])\qquad(3)$$

for $\phi \leq 0.95$. The OH· concentration as a function of the temperature alone can be established at the locations of the maximum OH· concentration and at greater radial locations where $\phi \leq 0.85$. Here there are no soot particles present, and the CO

concentration is either very low or undetectable (< 100 ppm). Figure 7 plots the temperature dependence of the OH· concentration in the methane/butane and the methane/1-butene flames. The steep gradients in both the OH· concentration and the temperature measurements require careful matching of their respective profiles for this analysis. The values of the OH· concentrations presented in Fig. 7 are averages of up to five measurements at the same temperature but for different radial profiles. The uncertainties in the OH· concentrations are estimated to be as much as ± 50% from the scatter of the values about their mean.

There are two major mechanisms which control OH· concentrations in the oxidation region of hydrocarbon diffusion flames, namely thermal quenching due to radiation losses (thermal effect) and reactions of OH· with soot particles and CO (chemical effect). These can be examined by comparing the [OH·] = f(T) data from Fig. 7 with [OH·] = f(T, [Soot], [CO]) for $\phi \leq 0.95$ obtained from the centerline profiles shown in Fig. 6. The methane/butane and the methane/1-butene flames have been selected for this correanalysis since the measured values of the local stoichiometry as a function of the axial location are closely similar in the two flames. If

$$F_1 = \frac{f(T)^1}{f(T)^2} \quad \text{and} \quad F_2 = \frac{f(T, [Soot], [CO])^1}{f(T, [Soot], [CO])^2}, \tag{4}$$

where the superscripts 1 and 2 represent the flames methane/butane and methane/1-butene, respectively, then the relative contribution

of thermal quenching to the observed decrease of the OH·
concentration in the methane/1-butene flame is the ratio F_1/F_2.

Table II summarizes the values of F_1, F_2, F_1/F_2 for three
temperature ratios T^1/T^2 at $\phi \leq 0.95$ in these two flames. Since a
common temperature regime was not available for $\phi \leq 0.95$ along the
centerline, a temperature ratio approach has been used. As this
temperature ratio increases, both F_1 and F_2 increase. However, the
ratio F_1/F_2 does not show any systematic change and is approximately
0.07, which indicates that the contribution of thermal quenching to
the observed decrease of the centerline OH· concentration is only
7% in the methane/1-butene flame. In light of the uncertainty in
establishing [OH·] = f(T), this value could be in error by ± 50%.
Nevertheless, this analysis indicates that the consumption of OH·
by soot and/or CO is mainly responsible for the low OH·
concentration in the interior of the methane/1-butene flame (see
Fig. 4).

C. Soot Oxidation Rates by OH· and O_2

An evaluation of the competition between soot and CO for
oxidizing species requires knowledge of their individual oxidation
rates, particularly due to OH·. The reaction rate for soot
particles can be expressed in terms of the temporal evolution of
the soot volume fraction:

where ρ is the density of the soot particles. This rate can also
be characterized from the time dependence of the d_{p30} profiles by

$$R_{Soot} = \rho \, \frac{df_v}{dt}, \tag{5}$$

substituting f_v from Eq. 1 into the above expression. Treating N_p as constant along a streamline and assuming $\rho = 1.8$ g/cm^3 (150 kmoles/m^3 for an atomic weight of 12) gives

$$R_{Soot} = 235.6 \, N_p d_{p30}^2 \, \frac{d_{p30}}{dt}, \tag{6}$$

where the units of R_{soot}, N_p, d_{p30}, and d_{p30}/dt are kmoles/m^3-s, cm^{-3}, cm, and cm/s, respectively. The number concentration of primary particles, N_p, calculated from consistent f_v and d_{p30} measurements, is almost a factor of two lower in the methane flame (2.1 x 10^{11} cm^{-3}) than that in the methane/butane and the methane/1-butene flames (3.7 x 10^{11} cm^{-3}). The slope of the d_{p30} profile as a function of time is evaluated from a combination of second, third, and fourth order polynomial fits. For the methane and methane/butane flames the fits also include the fact that the diameter of the primary particles must approach zero at the location of the visible flame tip (see Fig. 5). This procedure ensures a more accurate slope at the last temporal measurement locations. For the earliest time in the methane flame, however, the slope of the d_{p30} profile is quite uncertain since the primary particle size is expected to be close to its maximum value (see section III.B). Employing the fitting procedure just described in conjunction with Eq. 6 gives the net reaction rate (growth as well as oxidation) due to all species.

The soot oxidation rate can be obtained from the temporal evolution of the d_{p30} profiles only at locations where soot growth species (i.e., hydrocarbons) are absent. In this region, which is typically fuel lean, the soot oxidation rate due to OH· can be determined by subtracting contributions due to other oxidizing species. For the conditions of this study the equilibrium O-atom concentration is calculated to be 2-3 orders of magnitude lower than the equilibrium OH· concentration. Therefore, the relative contribution of O atoms to the total soot oxidation rate is expected to be small, even though superequilibrium O-atom concentrations are likely [19] and the collision efficiency for the oxidation of soot by O atoms is high [29]. In the present analysis the only oxidizing species considered are OH· and O_2.

Based upon these considerations, the soot oxidation rate due to OH· alone is given by:

$$\frac{d[Soot]}{dt}\Big|_{OH\cdot} = \frac{d[Soot]}{dt}\Big|_{meas} - \frac{d[Soot]}{dt}\Big|_{O_2} , \qquad (7)$$

where the oxidation rate due to O_2 is estimated from the NSC expression [3]. These OH· and O_2 contributions to the observed soot oxidation rate are presented in Fig. 8 and show that the contribution of O_2 to the observed soot oxidation rate is small throughout the oxidation region in all three flames studied.

Use of the Nagle and Strickland-Constable expression to estimate the O_2 contribution to the soot oxidation rate is subject

to some uncertainty. Numerous investigators have compared experimental oxidation rates of various carbons with the NSC expression and report rates that range between a factor of 20 lower to a factor of 6 higher than that given by NSC values. However, the trend in the reported comparisons suggests that the NSC expression overpredicts the O_2 contribution to soot oxidation at lower temperatures and possibly underpredicts at higher temperatures. Of particular interest is recent work on the oxidation of soot [30] and synthetic chars [31] by O_2 that indicates the use of the NSC rate expression overestimates the O_2 oxidation rate at temperatures below 1800 K. Note that the centerline temperatures in the methane, methane/butane, and methane/butene flames range between 1610-1798 K, 1494 - 1660, and 1236 - 1469 K, respectively (see Table I).

Chan et al. [30] studied the low temperature oxidation of soot in a propane diffusion flame and the oxidation of collected soot in an O_2/N_2 environment using an isothermal thermogravimetric technique. The oxidation rate of soot in the thermogravimetric study was an order of magnitude lower than that predicted by the NSC rate for a temperature of ~ 1100 K. At the same temperature these workers [30] report good agreement with the NSC rate for the diffusion flame study in which the soot oxidation rate was attributed completely to O_2 reactions. However, using an estimated equilibrium concentration of OH· for the conditions of their diffusion flame results in a soot oxidation rate (assuming a

collision efficiency of 0.1 [4]) that is 3 times faster than the NSC rate. Thus, it is likely that OH· reactions were important in their propane diffusion flame and the soot oxidation rate due to O_2 was overestimated by Chan et al. [30].

The work of Levendis et al. [31] on synthetic chars reports good agreement with the NSC rate only at higher temperatures (1800 - 2300 K). These workers observed oxidation rates to be 20 times lower than the NSC rate in the temperature range 800 - 1600 K. They ascribed the increase in reactivity of the chars above 1600 K to graphitization, which increased the total surface area. Felder et al. [32] also find the NSC expression to overpredict the oxidation kinetics of carbon blacks in the 1300 - 1700 K temperature range. In the upper temperature regime (i.e. above the apparent graphitization temperature of 1600 K reported by Levendis et al. [31]), Cadman et al. [33] report a factor of 6 higher soot oxidation rates compared to the NSC rate. In addition, Park and Appleton [34] justified the use of the NSC expression for soot oxidation based on shock tube experiments at higher temperatures (1700 - 4000 K). In light of these studies the use of the NSC rate probably overestimates the soot oxidation rate due to O_2 in the oxidation region of the flames investigated here. This would give a larger contribution of OH· to the observed soot oxidation rate, but the increase would be slight since the O_2 contribution is already small (Fig. 8).

D. Collision Efficiencies of OH· with Soot Particles

The soot oxidation rate due to OH· is often discussed from a fundamental kinetic theory viewpoint, which incorporates a collision efficiency parameter. This parameter is defined as the fraction of collisions that result in a carbon atom being removed from soot. Thus, the collision efficiency η is simply a means of matching the observed soot oxidation rates with the following expression obtained by considering OH· to be an ideal gas colliding with a soot surface:

$$R_{Soot} = \eta \, 4.6 \times 10^{18} d_p^2 N_p \, [OH·] \sqrt{T}. \tag{8}$$

Here R_{soot} is expressed in kmoles/m³-s and the units of d_p, N_p, [OH·], and T are cm, cm³, molecules/cm³, and degrees Kelvin, respectively. Estimates of the collision efficiency can be obtained by equating Eqs. 7 and 8.

Table III summarizes the values of η determined in the three flames at the various measurement locations. The asterisks denote either regions where soot particle growth is taking place (for example in the methane/butane flame) or regions where the estimated contribution due to O_2 is greater than the total soot reaction rate (in the methane/1-butene flame). The first data point in the methane flame yields a higher value for η than at later times. As mentioned earlier (section III.B), here the value of d_{p30} should be close to its maximum along the centerline, and thus the net soot reaction rate should be close to zero. The calculated values of η

are roughly constant for the methane flame, with the average value being 0.04.

In the methane/butane flame the collision efficiency shows an increase with time. The average of all the determinations is 0.08. For the methane/1-butene flame the collision efficiencies are found to be the highest. However, the first two values are unrealistically large and are likely to be in error due to the uncertainty in collecting samples across the high soot volume fraction annular region (see section III.B). Omitting these two values, the average collision efficiency between OH· and soot is 0.14.

The collision efficiencies determined for these flames fall within the range of values reported in prior investigations. Neoh et al., [4] measured an average value of 0.13 based on the primary particle size. The data of Roth et al. [35] exhibit large scatter for η, ranging from 0.1 to more than 0.3. Note that in both these studies the OH· concentration was not measured directly. Neoh et al. obtained the OH· concentration from a partial equilibrium estimate, and Roth et al. utilized the H_2/air mechanism given by Warnatz [36]. Mulcahy and Young [28] determined an effective upper limit of η for the gasification of carbon to be 0.08. These workers generated OH· by the following reaction:

$$H\cdot + NO_2 \rightarrow OH\cdot + NO$$
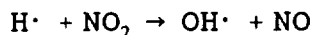
and obtained the OH· concentration by measuring the equimolar concentration of NO with a mass spectrometer.

The collision efficiency results described above reveal some interesting features. Not only do the derived collision efficiencies generally increase with time as soot oxidation proceeds, they also are larger in the flames with more soot. Figure 9 presents a striking correlation of the selected values of η with residence time which suggests that either (a) the soot particle reactivity changes with time, and/or (b) other oxidizing species are important. The inclusion of additional species in Eq. 7 would reduce both the soot oxidation rate due to OH· and its collision efficiency η.

The soot particle reactivity is known to change in the growth region of hydrocarbon flames [37-39]. This observation has been interpreted in terms of the concept of active sites. The growth of soot particles is argued [11] to accelerate after the inception region due to collisions of reactive species with the particle surface which produce active sites. At later times the reactivity of the soot particles changes due to thermal annealing or radical site stabilization processes [12,13]. The modelling results of Frenklach and Wang [40] indicate that the fraction of surface sites available for reaction (α) is lower at higher temperatures. They concluded that α is determined by steric effects, with the mobile

soot particle crystallites aligning themselves to limit access to gaseous species at higher temperatures. The collision efficiencies determined in the current study are plotted as a function of temperature in Fig. 10 and show more scatter than the η versus time results (Fig. 9). In terms of active sites, the collision efficiency should reflect the fraction of surface sites that are active (α). The variation of η with temperature shown in Fig. 10 is consistent with the modelling results of Frenklach and Wang, in terms of lower η at higher temperatures.

A second possible explanation for the apparent change in soot particle reactivity involves the presence of oxidizing species other than O_2 and OH· considered here. Dixon-Lewis et al. [5] have proposed a mechanism in which radicals catalyze attack by molecular oxygen. In their scheme the OH· radicals or O atoms, formed from the reaction of molecular O_2 with H atoms, attack carbon more effectively than O_2. This explains the observed increased rate of graphite oxidation in the main reaction zone of premixed flames. Figure 9 includes O_2 concentration data along with the calculated values of η as a function of time. The O_2 concentrations do not change substantially at early times (and at the higher temperatures). The H-atom concentration is expected to exhibit a maximum value near $\phi = 1.0$ [19]. Thus, the H-atom concentration should be decreasing for the last two points in the methane/butane flame and the three points in the methane/1-butene flame (see Table I). Although the data for the methane/1-butene flame show larger

O_2 concentrations, the temperatures are much lower and so is the expected H-atom concentration. Thus, the catalytic mechanism does not account for the observed increased reactivity over the whole range of experimental conditions.

In summary, the observed increase in the collision efficiency of soot oxidation by OH· with time most likely arises from an increasing reactivity of the soot particles. It is interesting to note that the flames that form more soot (possibly due to a larger fraction of active sites, α) also exhibit larger collision efficiencies with OH· . At this point one cannot determine whether the increased reactivity is a result of (1) the lower temperatures in more highly sooting flames and hence an increased fraction of surface sites available for reaction due to greater access to gas species, as proposed by Frenklach and Wang [40] or (2) that a greater number of active sites, which originate in the inception zone and produce a larger soot concentration, are still available in the soot oxidation region and are involved in oxidation reactions.

E. Competition for OH· between CO and Soot

The competition between CO and soot for OH· can be evaluated by comparing the soot oxidation rate computed from Eq. 8 with the forward rate of the CO + OH· reaction [41]:

where $d[CO]/dt$ is given in kmoles/m^3-s. The collision efficiency values for this analysis have been obtained from the linear least

$$\frac{d[CO]}{dt} = 1.5 \times 10^4 T^{1.3} e^{\frac{386}{T}} [CO][OH\cdot],\qquad(9)$$

squares fit shown in Fig. 9. Since both the CO and soot oxidation rates have a first order dependence on their respective concentrations, it is also appropriate to compare their normalized rates. If we consider

$$F_3 = \frac{\frac{d[CO]}{dt}}{\frac{d[Soot]}{dt}} \quad \text{and} \quad F_4 = \frac{\frac{1}{[CO]} \times \frac{d[CO]}{dt}}{\frac{1}{[Soot]} \times \frac{d[Soot]}{dt}},\qquad(10)$$

then the ratio F_3 is an indication of the amount of competition between CO and soot for OH·. For example, a value of $F_3 = 1$ implies an equal probability that an OH· molecule will react with CO or soot. The ratio F_4 reflects the intrinsic reactivity of OH· vs. CO and soot and is a function of the collision efficiency η, the primary particle size d_{p30}, and the temperature T (see Eqs. 1, 8 and 9):

$$F_4 \propto \frac{d_p T^{0.8} e^{\frac{386}{T}}}{\eta}.\qquad(11)$$

The direct dependence of F_4 on the primary particle size is intuitively understandable, since for the same soot volume fraction a smaller d_p will result in a larger soot oxidation rate due to the increased surface area. With increasing temperature the ratio F_4

increases due to a higher inherent reactivity of CO and a lower inherent reactivity of soot (smaller η).

Table IV summarizes the ratios F_3 and F_4 determined for the three flames at various values of the residence time. The methane flame shows the least competition between CO and soot for OH·, as reflected by the high values for F_3 and F_4. The OH· + CO rate is far larger than that for OH· + soot. This is due both to a low soot reactivity (Table III) and to the low soot concentration. As the soot concentration increases in the methane/butane and methane/1-butene flames, the competition between CO and soot for OH· increases. In the methane/1-butene flame, the soot oxidizes faster than CO at all but the two earliest residence times shown in Table IV. With increasing time in all of the flames, an increasing value of η increases the OH· + soot oxidation rate relative to the OH· + CO rate. This is reflected by the decreasing values of F_4 with time. Although CO is intrinsically more reactive with OH· than with soot in all the flames of this study (i.e., the F_4 values are all greater than 1), its oxidation is suppressed in the presence of large soot concentrations. This is most evident in the methane/1-butene flame.

V. CONCLUSIONS

Measurements of the hydroxyl radical concentration and the size of the primary soot particles have been made in a series of hydrocarbon/air diffusion flames containing varying amounts of soot. The observed OH· concentrations are suppressed in the presence of soot particles. A comparison of the fuel lean OH· concentrations in the presence and absence of soot particles reveals that the OH· concentration is reduced primarily due to reactions with soot rather than as a consequence of the lower flame temperatures measured for the higher soot loadings. The effect of lower temperatures on the OH· concentration is comparatively small, accounting for only 7% of the measured decrease in the OH· concentration.

The soot oxidation rates computed from the primary particle size profiles as a function of time reveal interesting trends for the soot particle reactivity. Higher collision efficiencies are deduced for the flames containing larger soot concentrations at lower temperatures. The variation of the collision efficiency with temperature is consistent with the modelling results of Frenklach and Wang [40].

A comparison of the soot and CO oxidation rates shows that although CO is inherently more reactive than soot on a per carbon basis, for large soot concentrations the soot successfully competes with CO for OH· and hence suppresses CO oxidation. The soot oxidation rates due to OH· were obtained by subtracting the

contribution due to O_2 (determined from the Nagle Strickland-Constable expression [3]) from the observed rates. Although the NSC expression is likely to overestimate the soot oxidation rate due to O_2 under the conditions of this study, the contribution of O_2 to the soot oxidation rate is found to be small compared to that due to OH·.

References

1. Puri, R., and Santoro, R.J., *Fire Safety Science - Proceedings of the Third International Symposium*, p. 595, 1991.

2. Fenimore, C.P., and Jones, G.W., *J. Phys. Chem.* 71:593 (1967).

3. Nagle, J. and Strickland-Constable, R.F., *Proceedings of the Fifth Carbon Conference*, 1:154, Pergamon Press, Oxford (1962).

4. Neoh, K. G., Howard, J. B. and Sarofim, A. F., *Particulate Carbon Formation During Combustion*, ed. Siegla, D.A., and Smith, G.W., Plenum, New York, p. 261 (1981).

5. Dixon-Lewis, G., Bradley, D., and El-Din Habik, S., *Combustion and Flame* 86:12 (1991).

6. Garo, A., Prado, G., Lahaye, J., *Combustion and Flame* 79:226 (1990).

7. Dobbins, R.A., and Megaridis, C.M., *Langmuir* 3:254 (1987).

8. Dobbins, R.A., Santoro, R.J., and Semerjian, H.G., *Twenty-Third Symposium (International) on Combustion*, The Combustion Institute, Pittsburgh, 1990, p. 1525.

9. Walker, P.L. Jr., Rusinko, F. Jr., and Austin, L.G.: Advances in Catalysis, 11:133, Academic Press, New York, 1959.

10. Howard, J.B., *Twenty-Third Symposium (International) on Combustion*, The Combustion Institute, Pittsburgh, 1990, p. 1107.

11. Tesner, P.A., *Combustion and Flame* 86:187 (1991).

12. Woods, I.T., and Haynes, B.S., *Combustion and Flame* 85:523 (1991).

13. Harris, S.J., *Combustion Science and Technology* 72:67 (1990).

14. Saito, K., Gordon, A.S., Williams, F.A., and Stickle, W.F., Combustion Science and Technology 80:103 (1991).

15. Toossi, R., *Combustion and Flame* 90:1 (1992).

16. Puri, R., Moser, M., Santoro, R.J., and Smyth, K.C., *Twenty-Fourth Symposium (International) on Combustion*, The Combustion Institute, 1992, p. 1015.

17. Santoro, R.J., Semerjian, H.G., and Dobbins, R.A., Combustion and Flame 51:203 (1983).

18. Smyth, K.C., Miller, J.H., Dorfman, R.C., Mallard, W.G., and Santoro, R.J., Combustion and Flame 62:157 (1985).

19. Smyth, K.C., Tjossem, P.J.H., Hamins, A., and Miller, J.H., Combustion and Flame 79:366 (1990).

20. Fairchild, P.W., Smith, G.P., and Crosley, D.R., J. Chem. Phys. 79: 1795 (1983).

21. Smith, G.P. and Crosley, D.R., J. Chem. Phys. 85: 3896 (1986).

22. Richardson, T.F., Doctoral Dissertation in preparation, Department of Mechanical Engineering, The Pennsylvania State University, 1992.

23. Puri, R., Richardson, T.F., Santoro, R.J., and Dobbins, R.A., Combustion and Flame 92:320-333 (1993).

24. Prado, G., Jagoda, J., Neoh, K., and Lahaye, J., Eighteenth Symposium (International) on Combustion, The Combustion Institute, Pittsburgh, 1981, p. 1127.

25. Megaridis, C.M., and Dobbins, R.A.: Combustion Science and Technology 66:1 (1989).

26. Köylü, Ü.Ö., Sivathanu, Y.R., and Faeth, G.M., *Fire Safety Science - Proceedings of the Third International Symposium*, p. 625 (1991).

27. Gordon, S., and McBride, B.J., "Computer Program for Calculation of Complex Chemical Equilibrium Compositions, Rocket Performance, Incident and Reflected Shocks, and Chapman-Jouguet Detonations", NASA SP-273 Interim Revision N78-17724, March 1976.

28. Mulcahy, M.F.R., and Young, B.C., Carbon 13:115 (1975).

29. S. von Gersum and P. Roth, Twenty-Fourth Symposium (International) on Combustion, The Combustion Institute, 1992, in press.

30. Chan, M.-L., Moody, K.N., Mulins, J.R., and Williams, A., Fuel 66:1694 (1987).

31. Levendis, Y.A., Flagan, R.A., and Gavalas, G.R., Combustion and Flame 76:221 (1989).

32. Felder, W., Madronich, S., and Olson, D.B., Energy and Fuels 2:743 (1988).

33. Cadman, P., Cornish, R., and Denning, R.J., Seventeenth International Shock Tube Symposium, 1990, p. 751.

34. Park, C., and Appleton, J.P., Combustion and Flame 20:369 (1973).

35. Roth, P., Brandt, O., Gersum, S. von., Twenty-Third Symposium (International) on Combustion, The Combustion Institute, Pittsburgh, 1990, p. 1485.

36. Warnatz, J., Ber. Bunsenges. Phys. Chem. 87:1008 (1983).

37. Harris, S.J., and Weiner, A.M., Combustion Science and Technology 31:155 (1983); 32:267 (1983); 38:75 (1984).

38. Bockhorn, H., Fetting, F., Heddrich, A., and Wannemacher, G., Twentieth Symposium (International) on Combustion, The Combustion Institute, Pittsburgh, 1984, p. 979.

39. Baumgärtner, L., Hesse, D., Jander, H., and Wagner, H.Gg., Twentieth Symposium (International) on Combustion, The Combustion Institute, Pittsburgh, 1984, p. 959.

40. Frenklach, M., and Wang, H., Twenty-Third Symposium (International) on Combustion, The Combustion Institute, Pittsburgh, 1990, p. 1559.

41. Wilk, R.D., Cernansky, N.P., Pitz, W.J., and Westbrook, K.C., Combustion and Flame, 77:145 (1989).

Table I: Summary of flame measurements obtained along the centerline and at the location of the peak OH· concentration for various heights H (cm) above the fuel tube exit. The OH· number densities, local stoichiometries ϕ, temperatures T, and superequilibrium ratios (SR) are shown. For the peak OH· results, a local stoichiometry of $\phi = 0.85$ has been assumed [16].

Flame	Centerline					Peak		
	H	ϕ	T	$[OH·]_{Ex}$	SR	T	$[OH·]_{Ex}$	SR
CH$_4$	7.62	1.21	1712	2.1E14	5.5	1748	1.0E16	6.2
	8.89	1.06	1774	2.2E15	14	1799	7.9E15	3.6
	10.2	0.99	1798	5.0E15	4.1	1742	5.7E15	3.6
	11.4	0.92	1690	4.9E15	4.8	1690	4.9E15	4.7
	12.7	0.84	1610	2.3E15	3.3	1610	2.3E15	3.3
CH$_4$/ C$_4$H$_{10}$	7.62	1.19	1494	1.5E14	69	1718	9.3E15	6.9
	8.89	1.06	1634	4.3E14	15	1658	7.4E15	8.0
	10.2	1.01	1660	1.6E15	16	1611	6.1E15	9.1
	11.4	0.96	1653	4.4E15	6.6	1610	4.7E15	7.1
	12.7	0.86	1549	2.8E15	6.6	1549	2.8E15	6.7
CH$_4$/ 1-C$_4$H$_8$	7.62	1.16	1403	8.2E13	154	1560	8.0E15	17.4
	8.89	1.06	1469	1.0E14	37	1444	5.8E15	32.2
	10.2	0.99	1435	2.0E14	2.2	1377	3.2E15	32.2
	11.4	0.93	1352	1.8E14	2.7	1293	1.8E15	43.0
	12.7	0.85	1283	4.6E13	1.2	1242	1.1E15	48.9
	14.0	0.77	1236	2.7E12	0.1	1192	5.3E14	42.2

Table II: Evaluation of the relative contribution of thermal quenching to the observed decrease in the OH· concentration along the centerline of the methane/1-butene flame.

T^1/T^2	F_1	F_2	F_1/F_2
1.19	1.86	22.9	0.08
1.22	2.25	24.2	0.09
1.28	3.72	93.6	0.04

[1]. Methane/Butane Flame;   [2]. Methane/1-Butene Flame

Table III: Summary of the collision efficiency, η, between soot and OH· obtained in the three flames at several times along the centerline streamline.

Methane		Methane/Butane		Methane/1-Butene	
Time (s)	$\eta_{OH·}$	Time (s)	$\eta_{OH·}$	Time (s)	$\eta_{OH·}$
0.114	0.122	0.119	*	0.126	0.648
0.117	0.043	0.122	*	0.131	0.374
0.120	0.030	0.124	0.044	0.137	0.134
0.122	0.050	0.127	0.065	0.141	0.100
–	–	0.129	0.070	0.146	0.182
–	–	0.132	0.079	0.151	*
–	–	0.134	0.144	–	–

– : No measurements; * : η for OH· cannot be determined.

Table IV: Summary of the ratio of the CO oxidation rate to the soot oxidation rate (F_3) and the ratio of the normalized CO reaction rate to the normalized soot oxidation rate (F_4) in the three flames.

Methane			Methane/Butane			Methane/1-Butene		
Time (s)	F_3	F_4	Time (s)	F_3	F_4	Time (s)	F_3	F_4
0.114	82.7	25.3	0.119	13.6	12.2	0.126	2.31	10.0
0.117	42.6	13.1	0.122	6.3	10.3	0.131	1.13	7.1
0.120	21.9	8.9	0.124	3.7	8.0	0.137	0.47	5.2
0.122	12.3	5.9	0.127	1.9	6.7	0.141	0.23	4.2
-	-	-	0.129	1.1	5.3	0.146	0.13	3.4
-	-	-	0.132	0.9	4.1	0.151	0.07	3.0
-	-	-	0.134	0.9	2.0	-	-	-

Figure Captions

Figure 1.   Schematic diagram of the laser-induced fluorescence experimental set-up.

Figure 2.   OH· concentration profiles in the methane/air diffusion flame at axial positions of 7.6, 8.9, 10.2, 11.4 and 12.7 cm from the fuel tube exit.

Figure 3. OH· concentration profiles in the methane/butane diffusion flame at axial positions of 7.6, 8.9, 10.2, 11.4 and 12.7 cm from the fuel tube exit.

Figure 4. OH· concentration profiles in the methane/1-butene diffusion flame at axial positions of 7.6, 8.9, 10.2, 11.4, 12.7 and 14.0 cm from the fuel tube exit.

Figure 5.   Comparison of the soot volume fraction, f_v (solid symbols), and the primary particle volume mean diameter, d_{p30} (open symbols) as a function of time along the centerline in the three flames.   The data for d_{p30} correspond to axial centerline positions of 7.6 to 9.5 cm in the pure methane flame (◇, ◆);7.6 to 11.4 cm in the methane/butane flame (□, ■); and 7.6 to 15.2 cm in the methane/1-butene flame (▽, ▼).   The arrows on the time axis denote the visible flame tip locations of the methane and the methane/butane flames.

Figure 6.   Centerline OH· concentration profiles in the three flames; the error bars denote statistical (see text) uncertainties only.

Figure 7.   The dependence of the OH· concentration on the temperature in the methane/butane and the methane/1-butene flames for $\phi \leq 0.85$ obtained at the location of the maximum OH· concentrations and in leaner flame regions.

Figure 8.   Plots of the observed centerline soot oxidation rate, shown as a solid line.   The contribution of O_2 as determined by the NSC expression (open symbols) and the derived (Eq. (7)) soot oxidation rate due to OH· (from Eq. 7; solid symbols connected by dotted curve) are shown for the pure methane (◇, ◆),the methane/butane (□, ■) and the methane/1-butene (▽, ▼) flames.

Figure 9.   Plots of the collision efficiency, η (solid symbols), and the O_2 mole fraction (open symbols) as a function of residence time along the centerline of the methane (◇, ◆),methane/butane (□, ■), and methane/1-butene flames (▽, ▼). The line is a linear least squares fit to the data.

Figure 10.   Plot of the collision efficiency, η, estimated from the soot oxidation rates and the OH· concentrations as a function of temperature in the methane (◆), methane/butane (■), and methane/1-butene (▼) flames. The line is a linear least squares fit to the data.
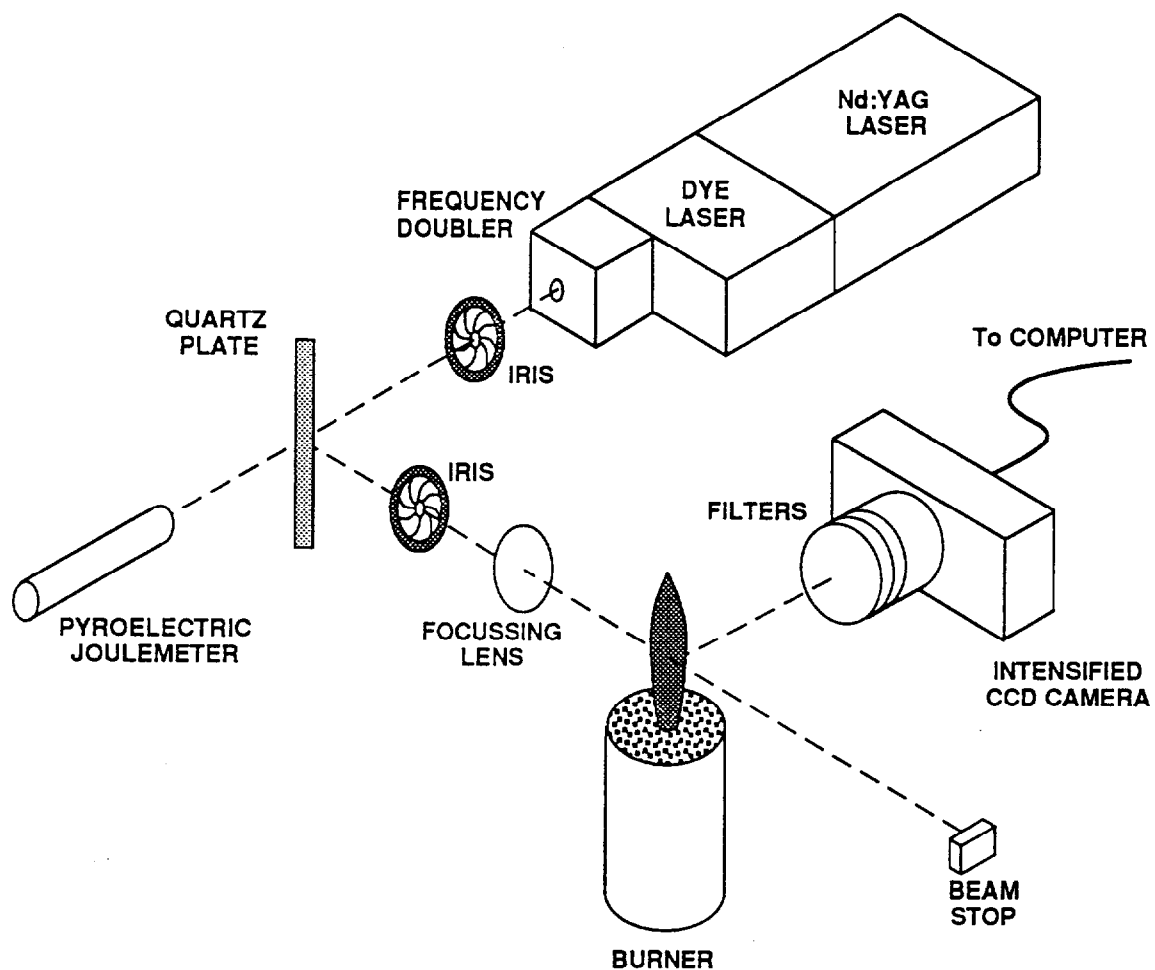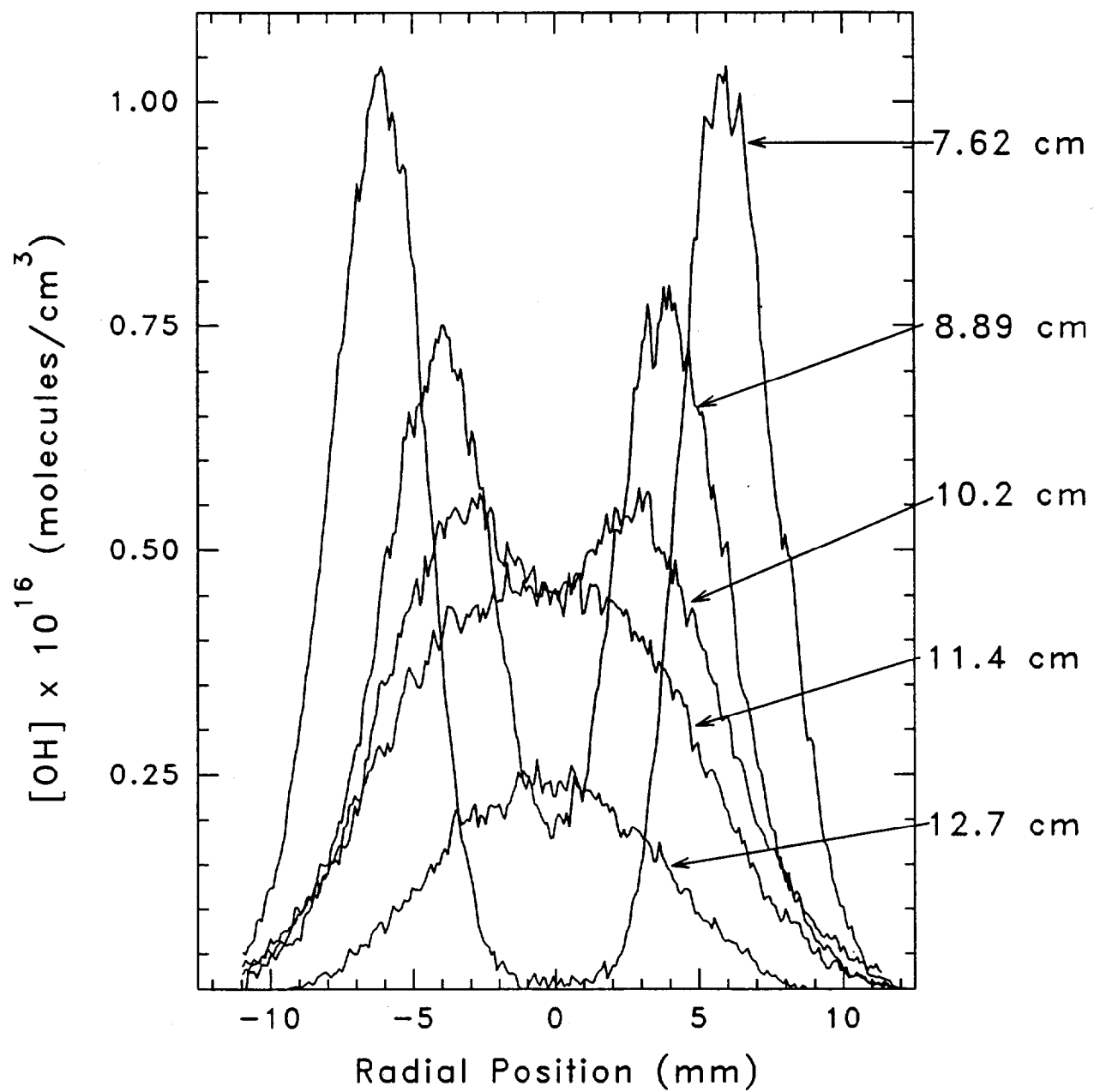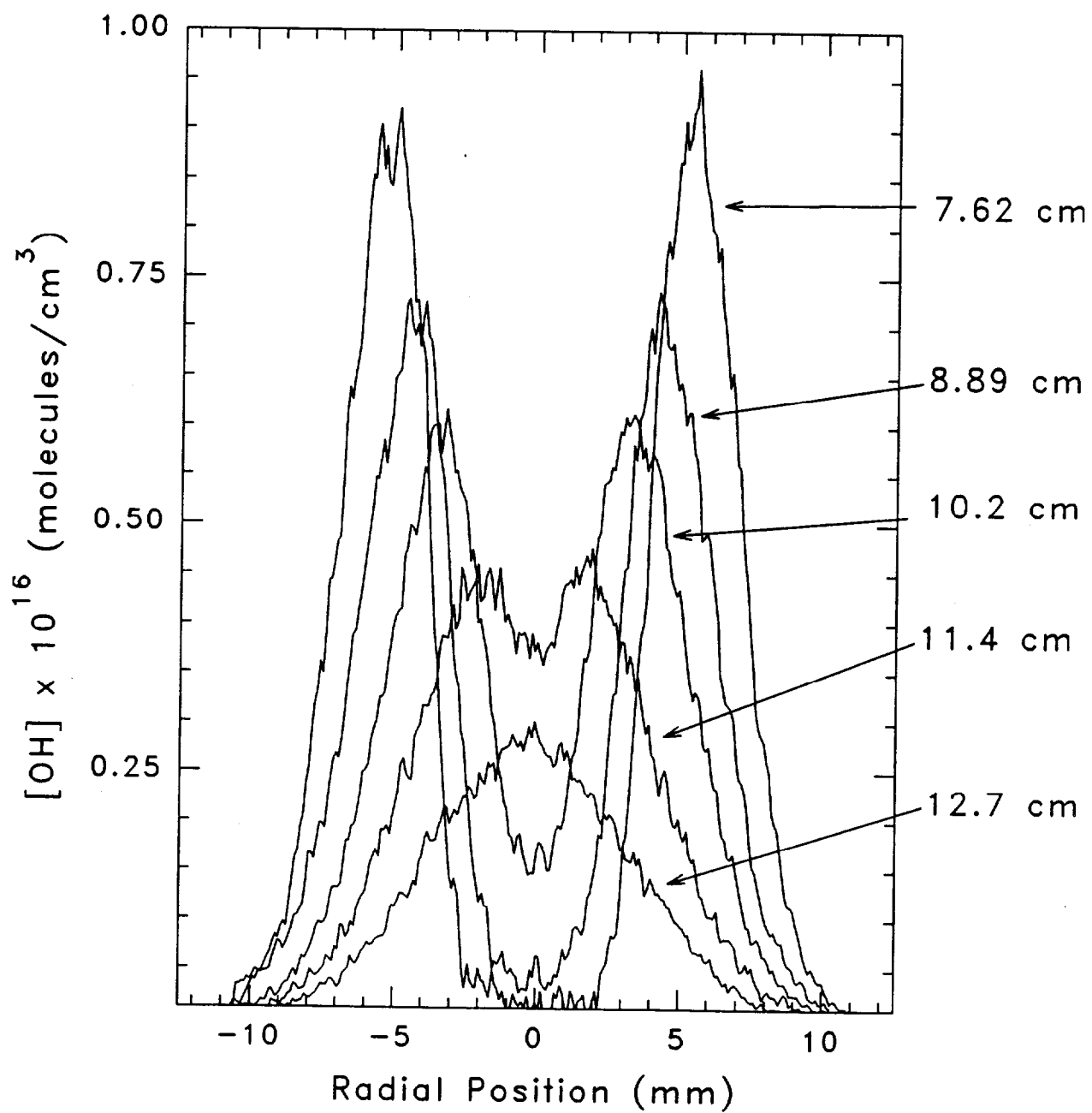
Fig. 1.   Schematic diagram of the laser-induced
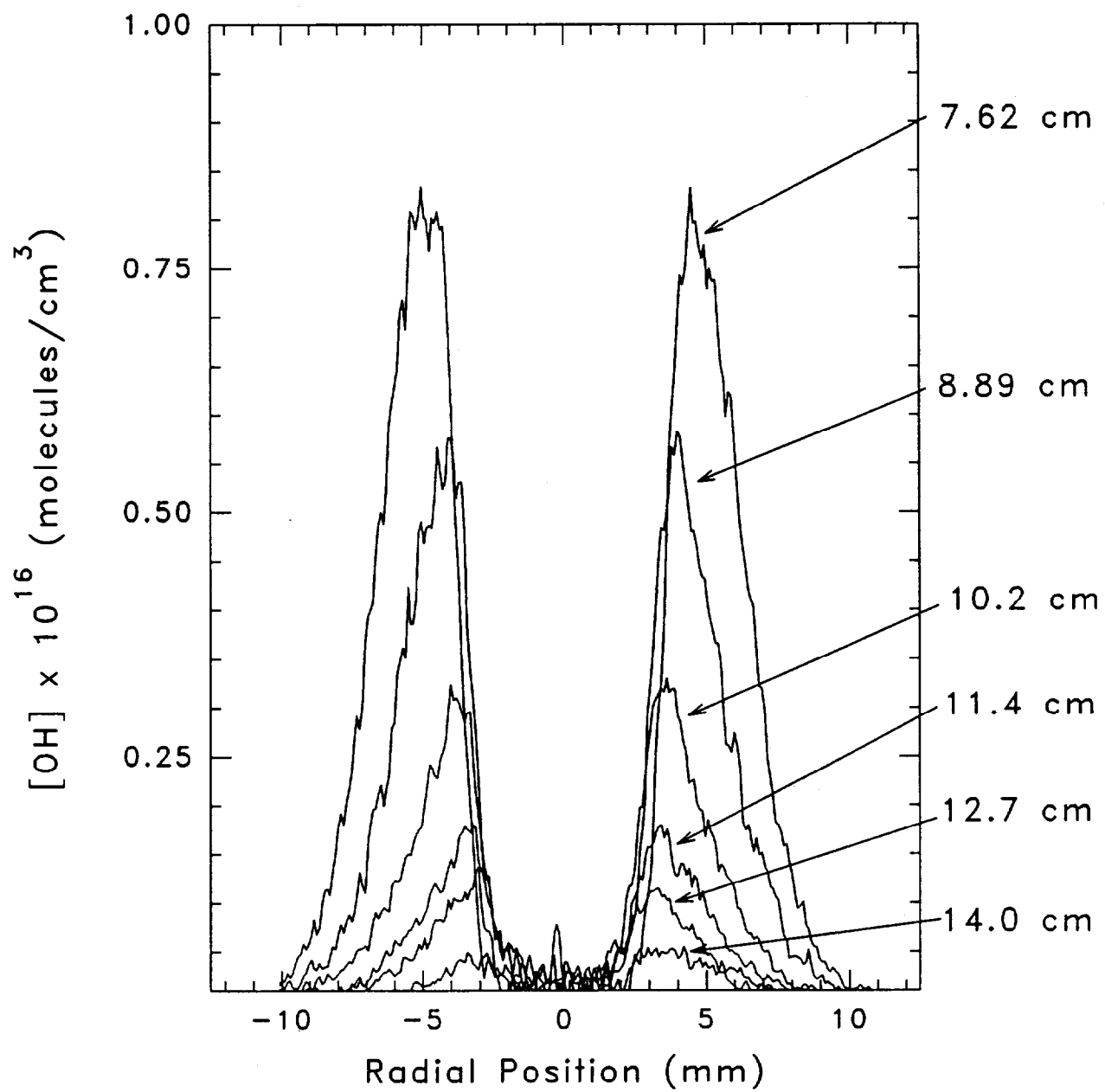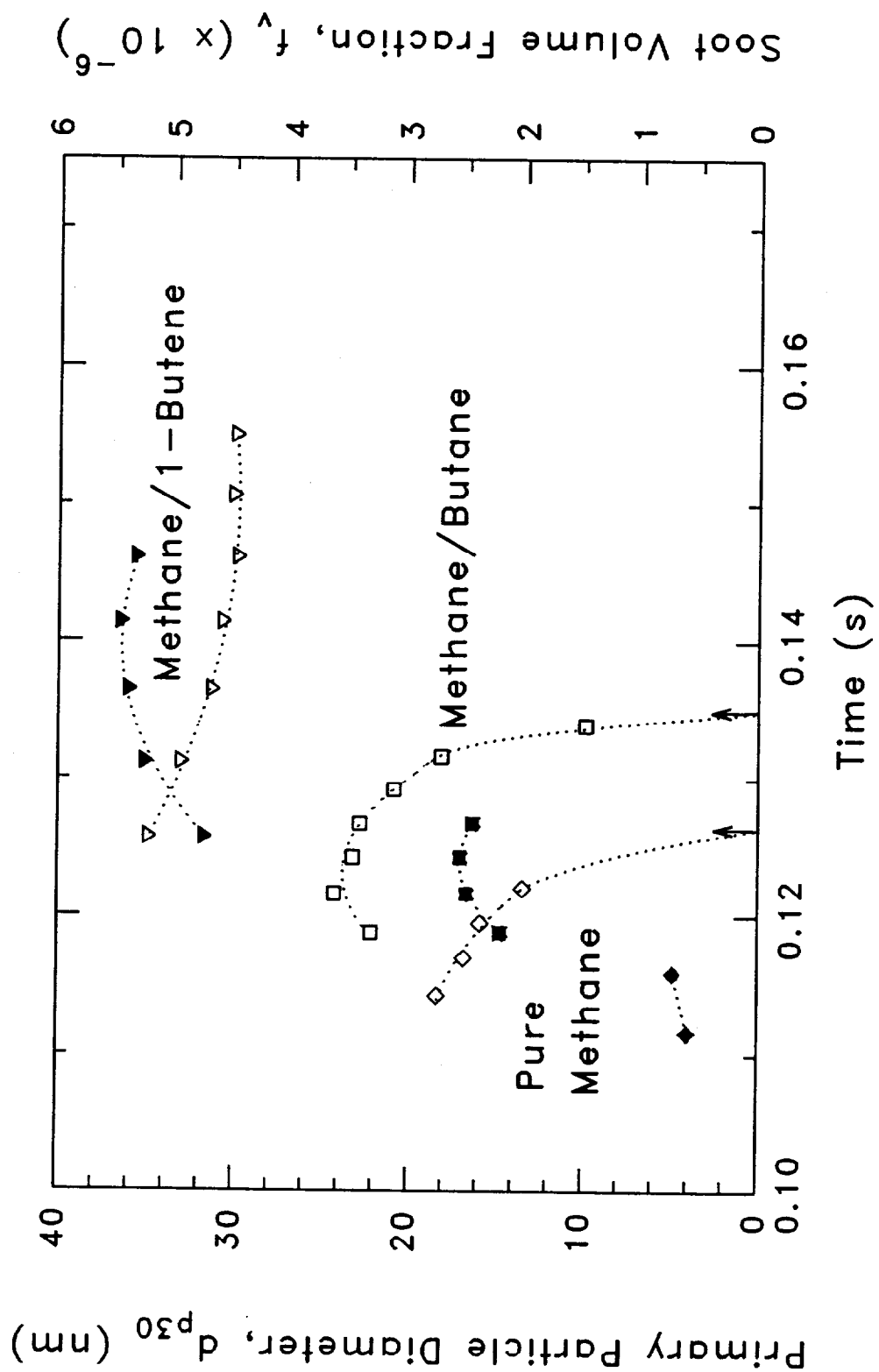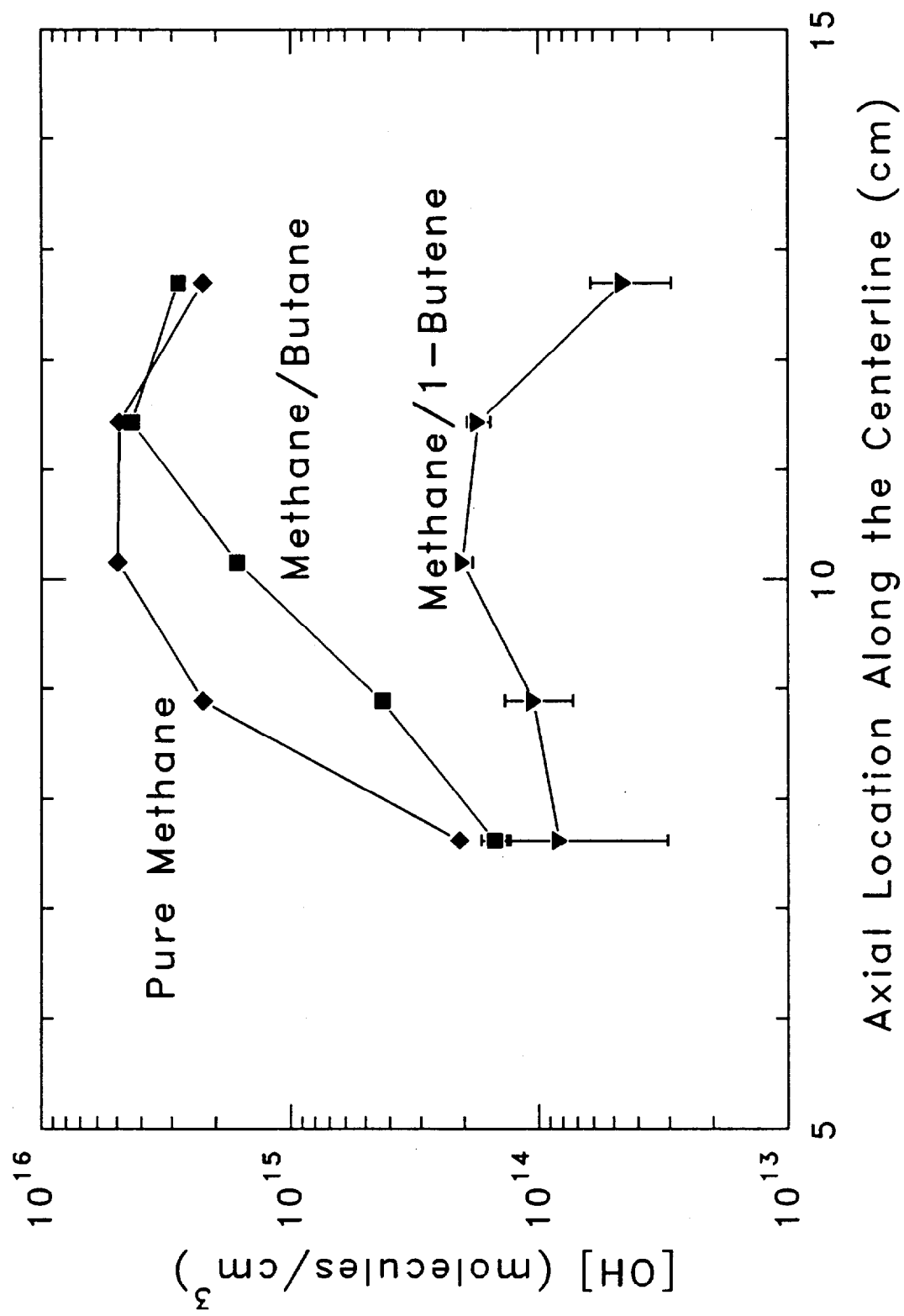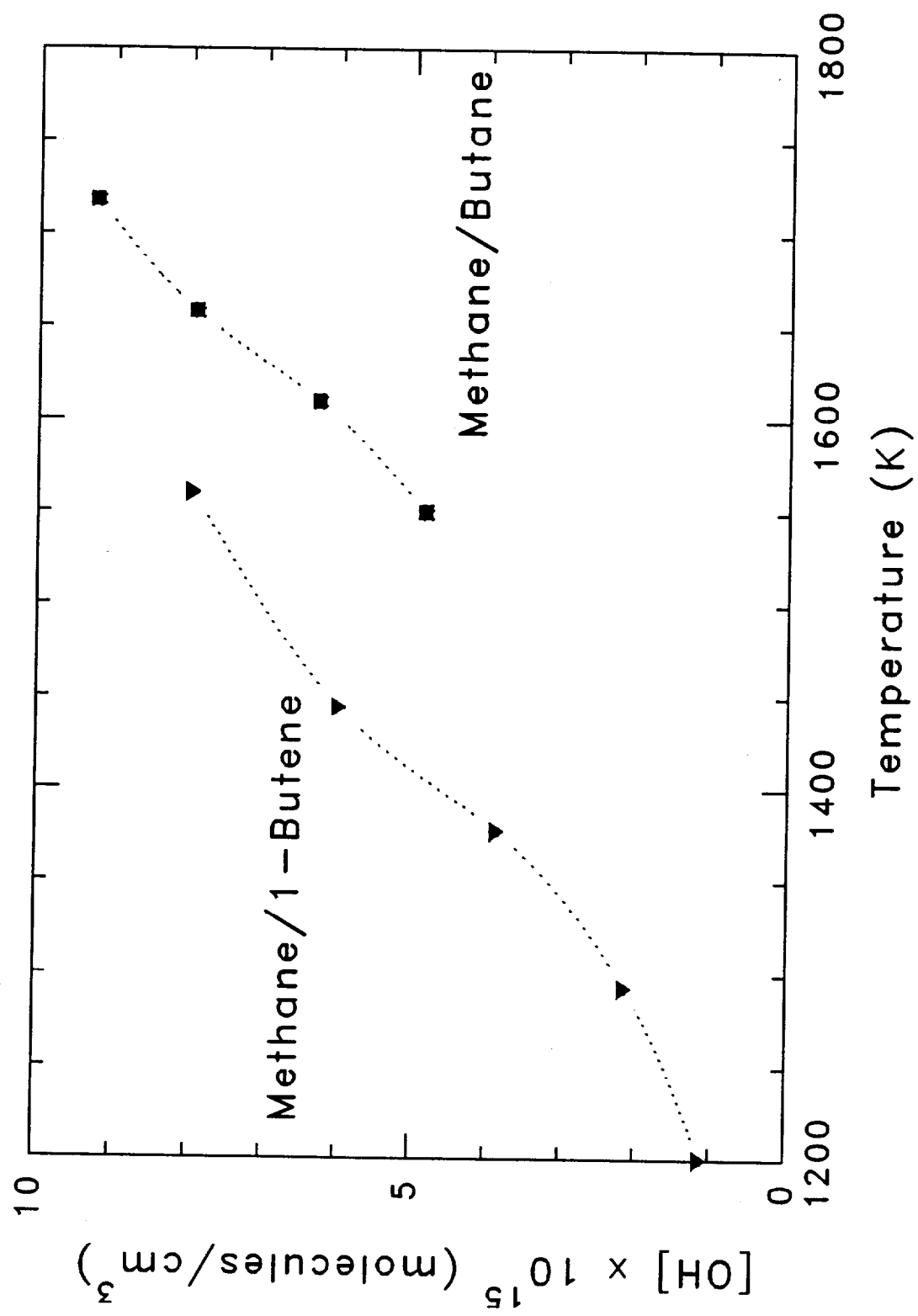   fluorescence experimental set-up.

The figure shows plots of $[OH] \times 10^{16}$ (molecules/cm^3) versus Radial Position (mm), with curves labeled 7.62 cm, 8.89 cm, 10.2 cm, 11.4 cm, and 12.7 cm.

Figure

Axis labels:
- y-axis: $[OH] \times 10^{16}$ (molecules/cm^3)
- x-axis: Radial Position (mm)

y-axis values: 1.00, 0.75, 0.50, 0.25

x-axis values: −10, −5, 0, 5, 10

Curve labels:
- 7.62 cm
- 8.89 cm
- 10.2 cm
- 11.4 cm
- 12.7 cm
- 14.0 cm

Soot Volume Fraction, f_v (x 10^{-6})

Time (s)

Primary Particle Diameter, d_{p30} (nm)
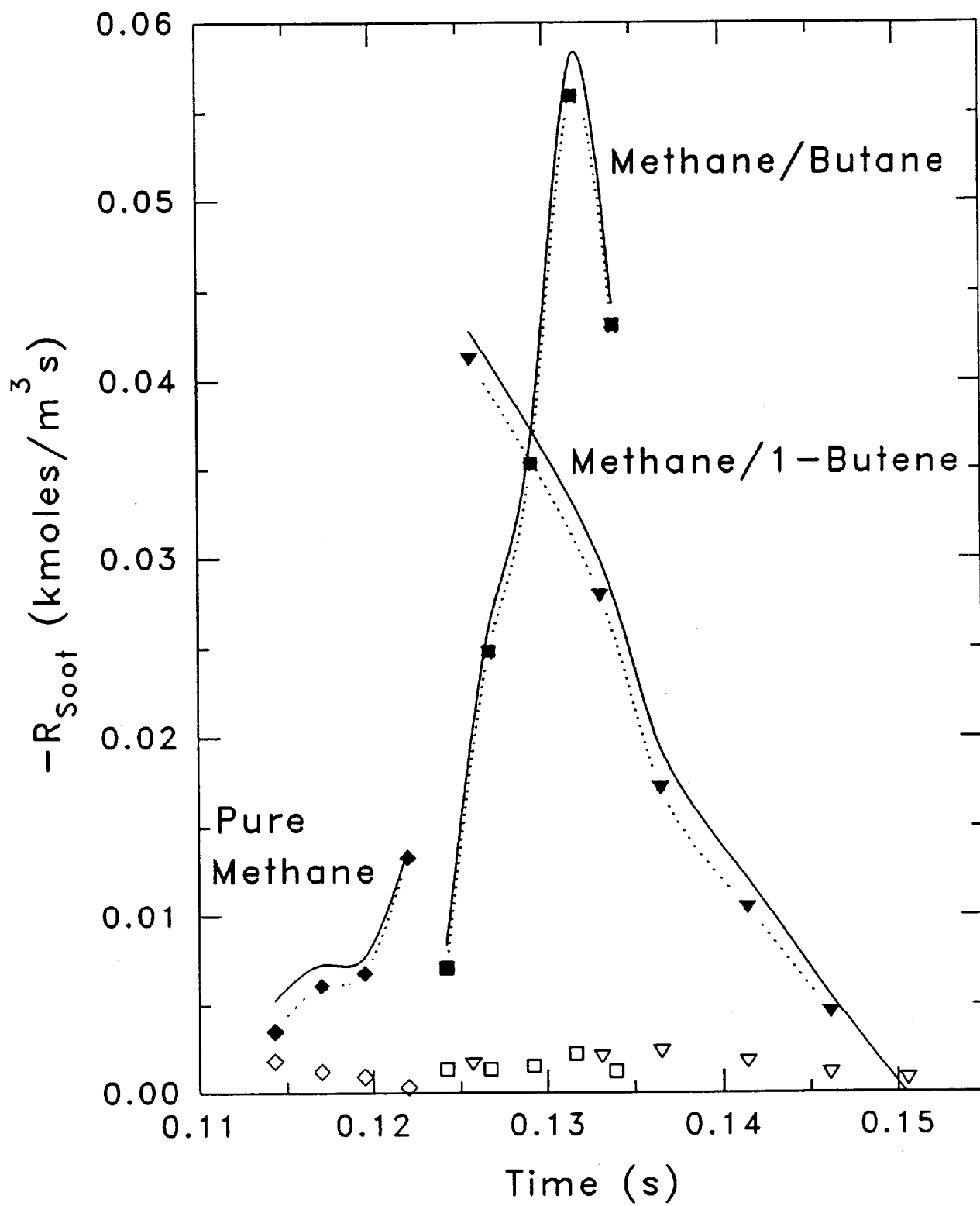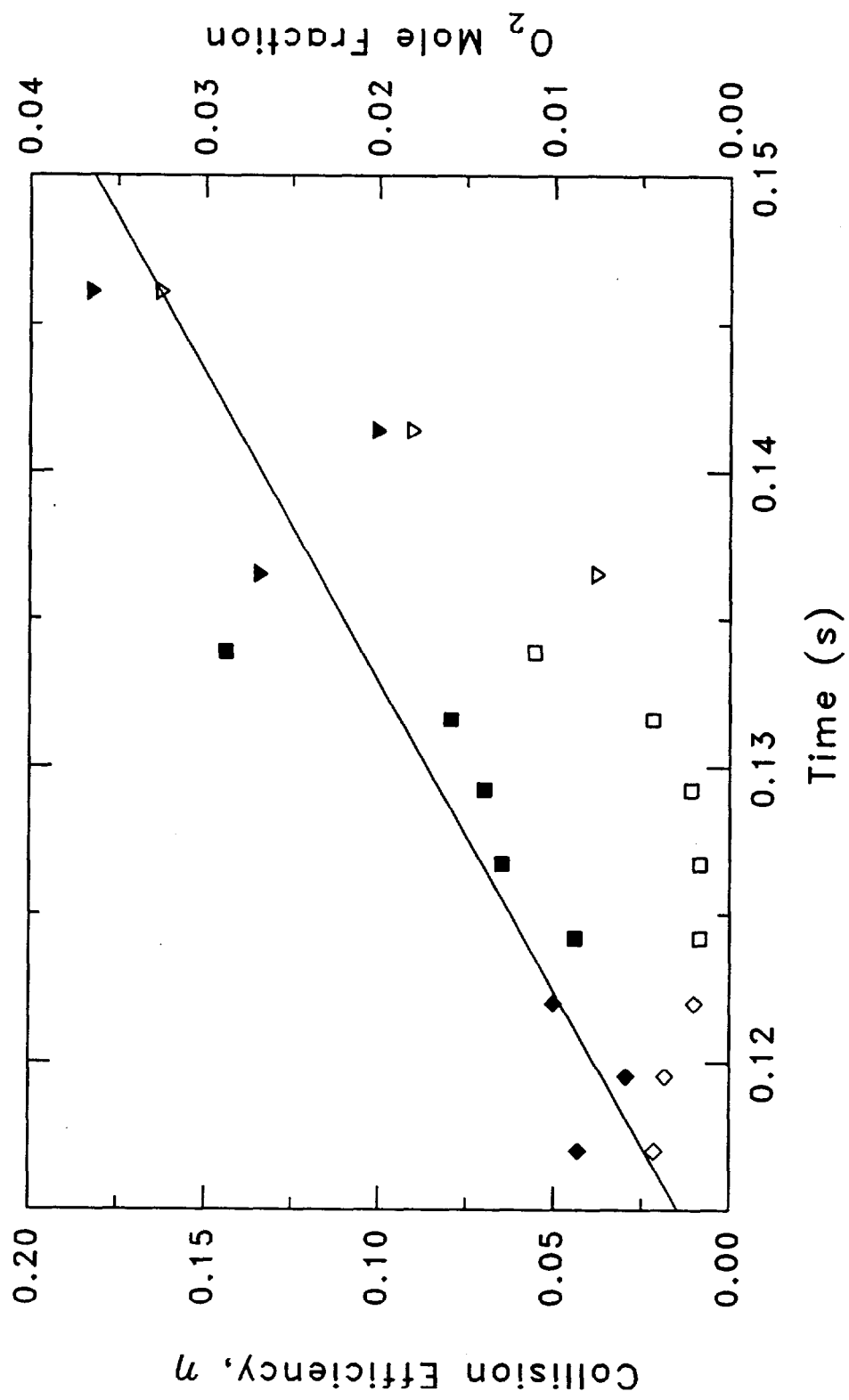
Methane/1-Butene
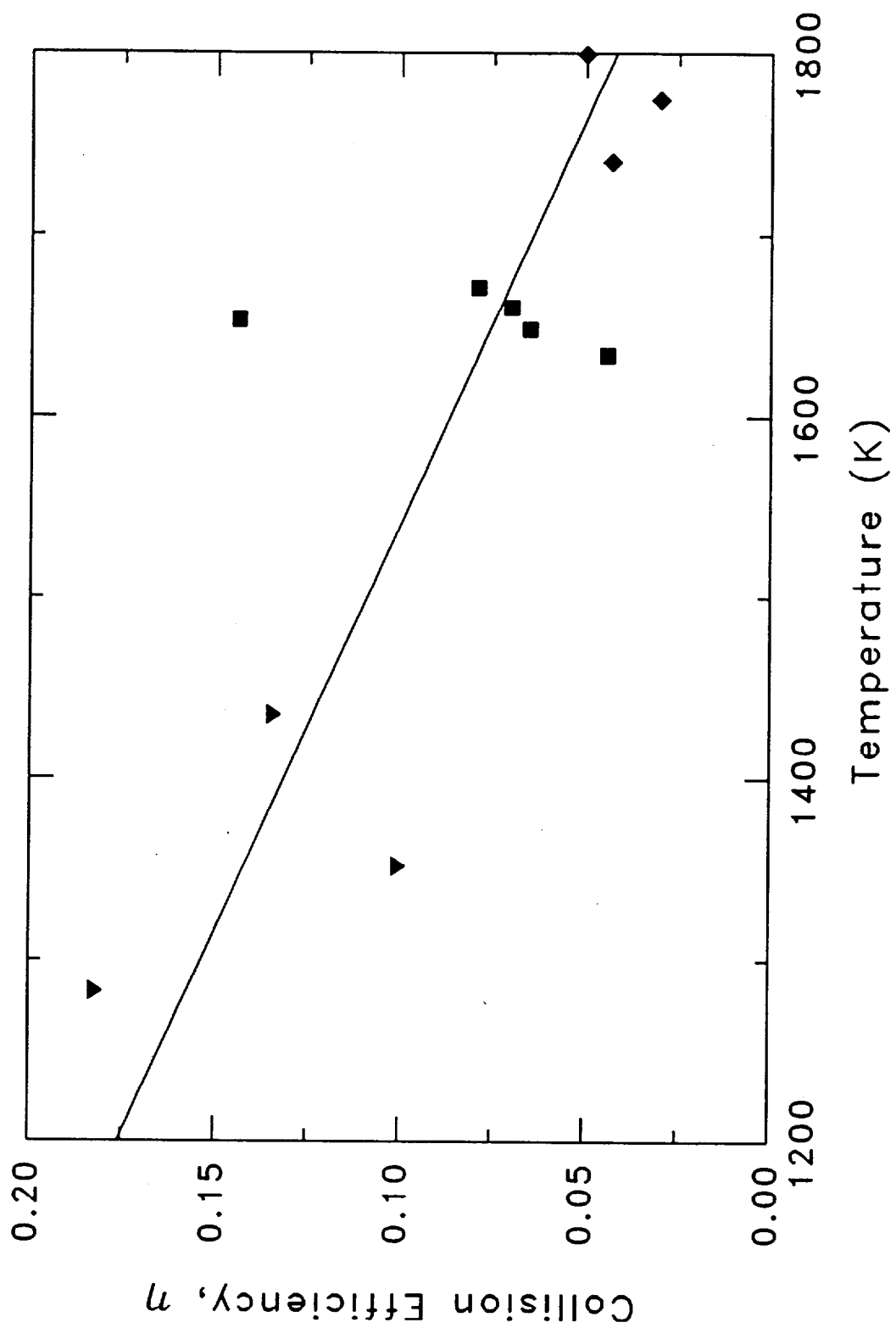
Methane/Butane

Pure Methane

Generation of CO and Smoke During Underventilated Combustion

S. Leonard, G.W. Mulholland*, R. Puri, and R.J. Santoro
Department of Mechanical Engineering
The Pennsylvania State University
University Park, PA 16802

Abstract - The CO and smoke yields observed for underventilated laminar diffusion flames are presented for methane and ethene for global equivalence ratio Φ over the range 0.5 to 4.0. A Burke-Schumann type burner with fuel in the center tube and air in the annular region was used. The peak CO yields for methane and ethene, 0.37 and 0.47 respectively, are at least a factor of 100 greater than for overventilated burning. The ratio of CO/CO_2 versus Φ for the methane flame is compared with local measurements of this ratio for both overventilated and underventilated laminar diffusion flames and with the results for turbulent natural gas flames quenched in an upper layer. The peak smoke yields for methane and ethene are 0.01 and 0.05, respectively, compared to yields of 0 and 0.028 for the overventilated case. The proportionality between smoke yield and CO yield observed for overventilated burning for a wide range of fuels is found not to be valid for the underventilated case. The chemical makeup and structure of the smoke produced at high equivalence ratio is qualitatively different from smoke produced under overventilated conditions; the smoke is mainly organic rather than graphitic and it has an agglutinated structure rather than an agglomerate structure with distinct primary spheres usually observed in overventilated burning.

---

* National Institute of Standards and Technology, Gaithersburg, MD, 20899.

INTRODUCTION

While there has been extensive research on overventilated laminar diffusion flames in terms of smoking height, yield of smoke and combustion gases, and species concentrations in the flame itself, there has been relatively little research on underventilated laminar diffusion flames beyond the work of Burke and Schumann [1]. Studies recently have been conducted of inverse laminar diffusion flames [2,3] which represent a closely related flame configuration. In these studies the oxidizer flow is surrounded by the fuel flow; the reverse of the normal laminar diffusion flame arrangement. There have been several studies of the species produced by underventilated turbulent flames [4-7]. In these studies the overall ventilation is controlled by adjusting the height of the collection hood relative to the burner. The fuels studied include methane by Toner *et al.*[4], methane, ethene, and propylene by Morehardt [5] and a variety of hydrocarbons, alcohols, as well as several polymers by Beyler [6,7]. In these studies there is an abrupt increase in the CO concentration as the global equivalence ratio, Φ, defined as the fuel-to-air ratio normalized by the stoichiometric fuel-to-air ratio approaches a value of 1.0. This large increase in CO is of concern in regards to safety implications for fires in structures and continuing research is underway to characterize the CO production during underventilated burning in enclosures [8,9].

The focus of the present study is to provide a quantitative data base on the production of CO and smoke particulates from laminar underventilated diffusion flames a la Burke Schumann [1]. Advantages of the underventilated laminar diffusion flame system include a wider range of Φ up to at least 4, the ease in measuring Φ and the yields of CO and smoke, and the potential for theoretical analysis of the generation rates of the combustion products. We have chosen methane, which is the simplest hydrocarbon and ethene, which has a moderate tendency to smoke. Methane [10-13] and ethene [14-17] are among the most carefully studied fuels for laminar overventilated flames. There are also data [4,5] for

CO concentration on turbulent underventilated flames for these gases. We are not aware of any quantitative study of smoke production during underventilated burning.

EXPERIMENT

A Burke-Schumann type burner [1] with fuel in the center and air in the annular region (Fig.1) was used in this study. In the Burke-Schumann study, the diameters of two concentric tubes were selected so that the air and fuel velocities were matched. If we were to maintain this condition in our study, a separate burner would be required for each value of Φ. Instead, we have used primarily two burner configurations. This simplifies the measurements and still allows us to assess the effect of the mismatch in the air and fuel velocities on the yield of CO and smoke. We have found that the qualitative trends in regard to the yield of CO and smoke as a function of Φ are insensitive to the velocity effect and, thus, focus this paper on a single burner configuration. Selected results are presented for a second burner configuration.

For overventilated ethene flames, there is an abrupt transition from non-smoking to smoking with a small change in fuel flow. For this reason, we have performed yield measurements for ethene flows corresponding to a non-smoking flame and to a smoking flame. While this produced a larger effect than changing the burner configuration, it still did not affect the qualitative trends. We focus our discussion on a single flow of 6.4 cm^3/s for ethene, which corresponds to a smoking flame for overventilated burning, and a flow of 10cm^3/s for methane. Selected results for a second flow of ethene are included.

4

Burner/Diluter Design

The burner design parameters and burner conditions are contained in Fig. 1 and Table 1. Most of the results presented in this paper relate to configuration 1. The burner housings were machined from 2" and 1" diameter brass. It was convenient to use nominal 3/8" (9.6 mm) and 1/2" (12.7 mm) brass tubing for the fuel tubes. The lengths of the fuel tubes, about 20 cm, were chosen long enough to ensure laminar flow at the outlet. The height of the fuel tube can be adjusted by loosening a compression fitting which is screwed into the base of the burner. Either burner tube (inner tube) could be attached to each of the two burner housings.

The air flow enters the base of the annular region, flows through a 2 cm layer of 3 mm diameter glass beads, and then through six layers of 70 gauge screen to provide laminar air flow. The inner glass tube (quartz) fits against the top of the screen located about 6 cm below the fuel tube. This quartz tube is sealed to the outer brass surface with teflon tape. The use of quartz enables one to burn off smoke deposits with a non-smoking methane flame as the outer surface is heated with a propane torch.

The outer glass tube , which serves as a concentric dilution tube, is sealed to the outer burner tube with a rubber stopper for the smaller burner housing and with an o-ring fit for the larger housing. The two dilution tubes were fitted with polished flanges to minimize leaks and to facilitate assembly. The purpose of the dilution tube is to provide uniform mixing of the smoke and gases and to cool the smoke particulate prior to collection. The nominal N_2 flow is 35.4 L/min (590 cm^3/s), which dilutes the combustion product by a factor of 2 to a factor of 30 depending on the combustion air flow. The combustion products mix with the N_2 as they pass through a tripper plate. Visual observation of scattered light from a laser beam passing through the diluted combustion products indicated that for a 2" (5 cm)

diameter tube a tripper plate with a 3/4" (1.91 cm) orifice provided good mixing at a dilution flow of 35.4 L/min (590 cm^3/s). The gas and smoke sampling position was located approximately 5 tube diameters downstream of the orifice. Subsequent gas sampling at seven uniformly spaced radial positions indicated a radial variation of less than 2% for both CO and CO_2. Variations in repeated measurements over the time period required for the radial profile were comparable to the apparent radial variation.

Two rotameters with overlapping ranges were used for the fuel flow and two for air flow to allow accurate flow monitoring over the range 2 to 20 cm^3/s for fuel and 10 to 280 cm^3/s for the air. Each flow meter was calibrated to an accuracy of about ±2% using soap film flowmeters with volumes of 1.0 L and 2.5 L and a dry test meter with a 10 L displacement. A nitrogen flow meter and filter collection critical orifice were also calibrated with the dry test meter. Precautions were taken to select the proper tubing size to minimize the pressure drop between the outlet of the flowmeter and the burner.

The dominant mechanism of smoke particulate deposition in this system is via thermophoresis, which is proportional to the temperature gradient near the wall. Cooling by rapid dilution by N_2 reduces the temperature gradient and consequently the particle deposition relative to cooling by only heat exchange with the walls of the tube.

Gas Analysis

The gas and particulate sampling systems are illustrated in Fig. 2. Both sampling inlets are located about 2.5 cm below the end of the dilution tube, which is covered with a screen to prevent backflow of air into the dilution tube. The gas sampling system consisted of a 1/4" (6.5 mm) diameter tube about 25 cm in length to provide some cooling before passing through a high capacity pleated filter.

The gases then flows through a 1 m length of 3/8" (9.5 mm) diameter copper tubing in a wet ice bath followed by about a 1.2 m length of tubing through dry ice. There was a drain cap in the wet ice bath to remove condensate. The flow then went through a displacement pump at a flow of about 0.8 L/min (13.3 cm^3/s) followed by through a NDIR CO analyzer and a NDIR CO$_2$ analyzer.

Standard calibration procedures were used with the gas analyzers involving zeroing the meters with dry N$_2$ and then spanning with known standards of 0.105% volume percent for CO and 5.03% for CO$_2$. The sensitivity of the CO meter is 0.001% and for the CO$_2$ meter is 0.01%. The measured values of CO during underventilated burning were in the range 0.07 to 0.5% while the CO$_2$ ranged from about 0.2% to 2%. The drift in the zero was on the order of the instrument sensitivity. A slight cross sensitivity of the CO meter to ethene was observed. This corresponded to an increase in the CO meter of 0.002% for a flow of 6.4 cm^3/s ethene and 35.4 L/min N$_2$ (590 cm^3/s), but no flame.

Our system afforded 3-4 hours of continuous operation before requiring thawing of the line going through the dry ice bath. In a typical measurement sequence, we would record readings for the two gas analyzers, change Φ by changing the air flow, and, after about a sixty second equilibration time, record the gas analyzer readings for the new condition. The detailed characterization for a given fuel involved 13 values of Φ equally spaced on a logarithmic scale between 0.5 and 4 and required about 1 hour to complete.

Smoke Particulate Analysis

The smoke sampling system consisted of a 5/8" (15.9 mm) OD stainless sampling tube 36 cm long, a 47 mm diameter filter holder, 3 m of 3/8" ((9.5 mm) diameter copper tubing, a critical orifice to control the flow, and a vacuum pump (see Fig. 2). The smoke sampling tube provided cooling of the gases from an inlet gas temperature of 200°C for the 10 cm^3/s methane flame burning at $\Phi=0.5$ to a temperature of about 100°C at the filter holder. For the other flame conditions, both the inlet and filter gas temperatures were lower. The cooling prevented deterioration of the polytetrafluroethylene (PTFE) coated filter. The collection efficiency for the filter (Pallflex** T60A) is reported [18] to be 70 to 80% for 0.035 μm diameter particles and at least 95% for particles with diameter of 0.3 μm and larger. The 3 m length of copper tubing assured that the gas temperature was at ambient conditions at the orifice. The vacuum pump operated at 1/10th of ambient pressure assuring a choked flow. The nominal flow through the filter was 9.2 L/min (153 cm^3/s). The flow was measured each day by attaching a dry test meter to the inlet of the smoke sampling system. Pressure gauges were attached for monitoring both the vacuum pressure and the pressure drop across the filter. The maximum pressure drop across the filter was 50" water (1.3 kPa) during the filter collection and this corresponded to about 15 mg of smoke collected on the filter.

** Certain commercial equipment, instruments, and materials are identified in order to adequately specify the experimental procedure. Such identification does not imply recommendation by the National Institute of Standards and Technology, nor does it imply that the materials identified are necessarily the best for the purpose.

8

Smoke collection required about five minutes after which the filter was removed and replaced with another preweighed filter. Typically one filter sample was collected for each of five different values of Φ during one set of measurements. The mass of smoke collected on the filter varied from about 0.1 mg to about 15 mg and in most cases exceeded 1 mg. Our filter weighings were repeatable to ±0.02 mg using a microbalance with a 0.01 mg sensitivity.

An estimate was made of the amount of smoke deposited on the tube walls relative to the amount collected on the filter. The smoke on the wall of the combustion tube was collected with a tissue attached to a plunger device. A second plunger arrangement was used for the dilution tube. Smoke was also collected from the orifice plate and the smoke sampling tube. The dilution tube accounted for most of the smoke deposition. Repeat measurements gave smoke depositions of 12 and 14%. These deposition measurements were made for the case of a relatively high gas temperature of 170°C. So we expect this estimate to provide an upperbound.

Filter samples were also collected at very light loadings on quartz fiber filters for analysis of the organic and elemental carbon fraction of the smoke versus Φ. This was done by a contract laboratory using thermo-optical analysis for organic/elemental carbon [19]. Smoke samples were collected for transmission electron microscopy on 3 mm diameter copper grids coated with a thin carbon layer. The grids were attached to a metal surface with double stick tape and held over the dilution tube exit for a period of one to 100 seconds depending on the smoke concentration.

FLAME STRUCTURE

Changing the value of Φ for a fixed burner configuration resulted in a mismatch in the air and fuel velocity. This differed from the Burke-Schumann study, where the air and fuel flows were typically matched. We generally obtained stable flames for the cases where the air velocity was greater than the fuel velocity, but we observed an oscillation of the flame at about 1 Hz when the air velocity was less than the fuel velocity. At an ethene fuel flow of 3.2 cm^3/s, the oscillation first appears at $\Phi=1.52$ for burner configuration 1. This corresponds to air velocity slightly larger than the fuel velocity. For larger fuel flows the oscillation is not apparent until a much lower relative air velocity; in fact, for $\Phi=4$ there is no oscillation in this case. Other qualitative features include the flame front bending below the burner for an ethene fuel flow of 3.2 cm^3/s, $\Phi=4$ for burner configuration 1 and flame blow off for methane at a fuel flow of 20 cm^3/s, $\Phi=0.7$ with burner configurations 2 and 3, which have the smaller diameter outer tube.

The effect of Φ on flame shape for the methane and ethene flames is illustrated in Fig. 3. For $\Phi=4$ the flame front is clearly curving toward the outer tube, though such a curvature is not clearly evident at $\Phi=1.52$. There does appear to be a slight necking in for $\Phi=1.52$, and this may signify the termination of the outward flame zone. A similar observation regarding the "central bright part of the flame rising above the actual flame" was made by Burke and Schumann in their original study[1]. The necking in of the luminous region observed in the present study is not attributed to the location of the reaction front, but rather to the transport of incandescent smoke particles. The actual reaction front should proceed to the wall as required for underventilated conditions[1]. The fact that the flame front does not extend to the wall of the burner makes the determination of a precise flame height difficult. Thus, we have taken the flame height for underventilated flames to correspond to the location where the flame begins to neck in.

We have included the predicted flame height based on Burke-Schumann theory using a diffusion coefficient of 0.60 cm^2/s, which corresponds to the diffusion coefficient of oxygen at 575 K. Roper[20] found that his data for circular port flames could be fit to the Burke-Schumann theory using this value of the diffusion coefficient. As previously pointed out the Burke-Schumann theory assumes equal air and fuel exit velocities, which enter into the theory through the air and fuel tube diameters. Since the exit velocities were not equal in the experiments, some adjustment had to be made to compare to the theory. For the present study the actual fuel tube diameter (9.6 mm) was used and an effective diameter for the outer air passage was calculated for use in the theory such that the air and fuel velocities were equal. The predicted flame height from the Burke-Schumann analysis is greater than the blue zone, but is clearly less than the maximum luminous height (see Fig. 3). The increase in flame height with decreasing Φ is qualitatively predicted by the Burke-Schumann theory. The flame shapes are qualitatively similar for both the methane and ethene flames, but the much more intense luminous radiation from the smoke in the flame is apparent for the ethene case. Long exposure times were required for the ethene flames to bring out the bluish reaction zone presumably arising from CH radicals.

CO AND SMOKE DATA ANALYSIS

The measured volume % of CO and CO_2 in the diluted gases on a dry basis are plotted versus Φ in Fig. 4 for the methane flame at a fuel flow of 10 cm^3/s and include a set of repeat measurements several weeks apart. An equal spacing of points on a logarithmic scale in Φ was used to provide both good coverage near the rapidly changing region around $\Phi=1.0$ and coverage over the entire range from $\Phi=0.5$ to $\Phi=4.0$. We see from Table 2 that the volume % for CO, X_{CO2}, increases from 0.001 (the minimum detection limit for the CO analyzer) to 0.31 as Φ increases from 0.76 to 1.32. The 0.31% CO

for the diluted combustion products corresponds to an estimated 2.5% CO prior to dilution with nitrogen. This estimate is based on the flows of nitrogen, methane, and air (Table 2). The estimated peak CO concentration prior to dilution with nitrogen is 2.9% at $\Phi=2.0$.

It is convenient to express the results in terms of the yield, ε, on a mass basis, where ε_{CO} is equal to the mass of CO produced per mass of fuel entering the burner. The procedure for determining the yield is outlined below. First the volume flow of CO, F_{CO}, is computed from the measured volume % of CO, X_{CO}, and the total volumetric flow through the dilution tube, F_T, corrected to ambient conditions.

$$F_{CO} = \frac{X_{co}F_T}{100} \quad . \tag{1}$$

Next the density of CO, ρ_{CO}, is obtained from the ideal gas law as

$$\rho_{CO} = \frac{M_{co}P_A}{RT_A} \quad . \tag{2}$$

where M_{CO} is the molecular weight of CO and the subscript A refers to ambient conditions. From eqs.(1) and (2) we obtain the total mass flow of CO, $\dot{m}_{CO}$, as

$$\dot{m}_{CO} = \frac{X_{co}F_T}{100}\frac{M_{co}P_A}{RT_A} \quad . \tag{3}$$

To compute the yield of CO we also need the mass flow of fuel, which is obtained from the volumetric flow of the fuel, F_F, and its density, ρ_F. Using an expression similar to eq.(2) for computing the density, we obtain the following expression for the mass flow of fuel:

$$\dot{m}_F = F_F \frac{M_F P_A}{R T_A} \quad . \tag{4}$$

The yield of CO, ϵ_{CO}, is obtained from eqs.(3) and (4) as the ratio of the mass flow of CO to the mass flow of fuel.

$$\epsilon_{CO} = \frac{\dot{m}_{CO}}{\dot{m}_F} = \frac{X_{CO} F_T M_{CO}}{100 F_F M_F} \quad . \tag{5}$$

The above expression requires that the fuel and combustion products are at, or are corrected to, the same temperature and pressure.

In Eq.(5), we approximate the total volumetric flow F_T as the sum of the volumetric flows of N_2, fuel, and air. This is a good approximation since the volumetric flow of N_2 accounts for at least 94% of the inlet flow for both the methane flame at a flow of 10 cm^3/s and the ethene flame at a flow of 6.4 cm^3/s for all values of Φ measured for a typical dilution flow of N_2 of 35.4L/min (590 cm^3/s). Furthermore, for both methane and ethene, the sum of the number of moles of CO_2 and H_2O produced by complete combustion is equal to the sum of the number of fuel and oxygen moles. For Φ less than or equal to 1, complete combustion is a good approximation. For $\Phi > 1$ there is a significant amount of CO and possibly H_2 produced in addition to H_2O and CO_2; however as Φ increases, an increasingly large percentage of the inlet flow is N_2. For $\Phi = 1.5$, 97% of the inlet flow is N_2 for the two fuel flows given above. The production of smoke will result in a reduction in the outlet gas flow; however, even if 10% of the fuel carbon becomes smoke for ethene, which is greater than any value we measured, the reduction in the volumetric flow is only 0.1% for $\Phi = 1$.

So we see that for $\Phi > 1$, the above flow approximation is valid to within about 3%. One other factor plays a role for Φ in the range 0.5-1.0; that is, the fact that the water produced by the combustion

is removed by the wet and dry ice traps. Assuming complete combustion and assuming all the water is removed by the cold traps, we find that the total flow is reduced by 2.9% for methane at 10 cm^3/s and 1.9% for ethene at 6.4 cm^3/s. We conclude that approximating F_T as the sum of the N_2, air, and fuel flow is valid to within 3%. Below we provide a consistency check of this approximation.

The other quantity of interest is the smoke yield, ε_S, which is determined from the mass flow of smoke to the filter, $\dot{m}_S$, the mass flow of the fuel $\dot{m}_F$, and the volumetric dilution factor, f_{dil}, which is equal to the ratio of F_T to the volumetric gas flow through the filter, F_f.

$$\epsilon_s = \frac{\dot{m}_S}{\dot{m}_F} f_{dil} \quad . \tag{6}$$

Typical results for methane at a fuel flow of 10 cm^3/s and ethene at 6.4 cm^3/3 are given in Table 2. We see that the repeat CO yield measurements for $\Phi \geq 1.52$ agree within 2%; the large difference at $\Phi = 1.0$ results from the great sensitivity of yield to Φ near $\Phi = 1$.

An estimate of the accuracy of our method for computing gaseous yields can be made by comparing measured CO_2 yield for $\Phi = 0.5$ with the predicted CO_2 yield for complete combustion for methane and ethene. For overventilated burning such as this the major product of combustion is CO_2. For methane at $\Phi = 0.5$, the measured yields are 1-3% less than the predicted value of 2.75 while for ethene the measured values are 7-8% less than the predicted value of 3.14. From the CO_2 analog of Eq.(5) we estimate an overall uncertainty of $\pm 6\%$ by combining the uncertainties associated with volume fraction and flow measurements. The methane results are within the expected uncertainty range, while the ethene results are slightly outside the range. However, for ethene 2 to 3% of the fuel carbon becomes smoke particulate at $\Phi = 0.5$ so perfect agreement with the predicted value of 3.14 is not expected. If we compute the total amount of carbon in the combustion products including CO, CO_2, and smoke assuming

the smoke is carbon, we find that the computed amount is 6% less than the amount of carbon in the fuel for the ethene flame data in Table 3. This comparison leads to an uncertainty estimate for CO yield of $\pm6\%$ near the peak, a somewhat larger uncertainty at $\Phi=4$ because of the decrease in the CO volume fraction, and a large uncertainty on the order of $\pm50\%$ at $\Phi=0.5$ because the CO volume fraction is comparable to the instrument noise.

The measured smoke yields are an underestimate by 20 to 25% because of the estimated 13% wall deposition and a nominal 10% penetration of the smoke through the filter. The estimated repeatability of the smoke yield results, $\pm8\%$, is more variable than for the CO yield, because one additional flow (smoke sampling flow) is needed and because of the variability associated with particle deposition and penetration.

CO AND SMOKE YIELD RESULTS

The CO yield increases abruptly with Φ to a peak value of 0.37 for methane and 0.47 for ethene. As shown in Fig. 5, the peak in the methane curve occurs at a slightly smaller Φ than for ethene, 1.3 relative to 1.7. It is seen that repeat measurements agree within about $\pm5\%$ for values of $\Phi>1$. The CO yield is very sensitive to small changes in Φ near $\Phi=1$ and larger differences are obtained for repeat measurements near $\Phi=1$. Additional measurements were performed at other fuel flows and with a second burner configuration to determine the generality of this shift and the results were inconclusive in regard to the difference being attributed to fuel chemistry. As indicated in Fig. 6, decreasing the fuel flow for ethene by a factor of two to 3.2 cm^3/s shifts the peak to the left by an amount similar to the difference between ethene at 6.4 cm^3/s and methane at 10cm^3/s.

The smoke yield curve peaks at smaller Φ, near 1.0, compared to the result for CO as shown in Fig. 7. Also for large Φ, the percentage decrease for smoke is much greater than for CO. This will become more apparent when the results are presented in an alternative form in the discussion session. While the repeatability of the smoke yield measurements is not as good as that of gas yields, still the results are consistent with our predicted repeatability of $\pm 8\%$. The same general curve shape was obtained with methane as ethene as shown in Fig. 8 though the ethene peak is about 5 times greater than the peak for methane.

The smoke yield decreases sharply for $\Phi > 1.5$ as shown in Fig. 9 as the fuel flow decreases. This is the same trend as for CO (see Fig. 6). The large reduction in the smoke yield at $\Phi = 0.5$ is expected since the fuel flow is below the smoke point for the overventilated flame..

As discussed in the first section, we performed experiments on several different burner configurations. Here we show results on two configurations. In the second configuration the quartz tube is smaller making the air velocity about a factor of two greater than in the first. The yields are qualitatively similar for the two burner configurations as shown in Fig. 2. Increasing the air velocity results in a slight increase in the CO yield but a slight decrease in the smoke yield. There is a surprising result at $\Phi = 0.5$ that the smoke yield goes to zero for the higher air velocity even though the fuel flow is well above the smoke point.

We noticed from the filter samples that the smoke generated at large Φ appeared lighter in color and that the deposit on the combustion burner tube had a liquid character. In fact, for methane at $\Phi = 4$, the filter had a yellowish appearance. Thermo-optical analysis of the smoke collected on the quartz filters indicated that as Φ increased the organic fraction of the smoke increased relative to the elemental carbon

fraction. As indicated in Table 3, at $\Phi=4$ for both fuels the organic fraction is greater than the elemental fraction. This is in sharp contrast to the results at $\Phi=1$ and $\Phi=0.5$ where less than 10 percent of the smoke is organic carbon.

Additional evidence of the difference in character of the high Φ smoke compared to the low Φ smoke are the electron micrographs (Fig. 11) of the ethene smoke collected at $\Phi=4$ and $\Phi=1$. We see that while in both cases the smoke has an agglomerated structure, at $\Phi=4$ the agglomerate is agglutinated indicating the presence of a liquid-like component. A Phillips 420T transmission electron microscope was used at a voltage of 100kV with a 60,000 X magnification.

DISCUSSION

The discussion is focussed on the results for underventilated burning, but our new finding for overventilated burning that increasing the velocity of air relative to the fuel velocity changes a smoking ethene diffusion flame to a non-smoking flame invites notice.

The peak CO yields for methane and ethene differ by only 20%, while the peak smoke yields differ by about a factor of five. This result that the CO and smoke yields seem uncorrelated for underventilated burning differs markedly from the strong correlation between CO and smoke yields for overventilated burning observed by Koylu *et al.* [21] for gaseous hydrocarbon fuels and Mulholland *et al.* [22] for plastics and lumber.

One difficulty with the definitions of CO and smoke yields given by eqs.(5) and (6) is that as Φ increases much of the fuel is not involved in the reaction. A better normalization in regard to analyzing

chemical effects is the CO yield per g of fuel consumed or per g of oxygen consumed. Here we compute the yield based on oxygen consumption because the data analysis is simpler in this case. For $\Phi \geq 1$, the oxygen consumed is estimated from the inlet flow of oxygen. This is a good approximation, since essentially all the oxygen will react for fuel rich burning. For $\Phi < 1$, we compute the mass flow of oxygen consumed from the product of the fuel flow and Φ. This is a good approximation, since CO_2 and water account for at least 95% of the combustion products for fuel lean burning. As shown in Fig. 12 and Fig. 7, the CO yield per g O_2 consumed varies much less for $\Phi > 1.5$ compared to the CO yield per g fuel entering the burner. The ratio of the maximum to the minimum yield of CO over the Φ range, $1.5 < \Phi < 4$, is 1.3 per g O_2 consumed and 2.6 per g of fuel entering the burner.

It is of interest to consider local measurements for laminar methane flames for overventilated burning by Mitchell et al. [10] and for underventilated burning by Puri [23] to obtain insight regarding our result of a nearly constant yield. The comparison will be made in terms of the ratio of the volume % of CO to the volume % of CO_2, since all the data needed for computing yield is not available. This ratio is a useful parameter for assessing changes in flame chemistry, since CO and CO_2 comprise the major carbon containing products of combustion. The ratio X_{CO}/X_{CO2} obtained in each of these studies is relatively constant with a value of 0.6 over the local equivalence ratio range $1.5 < \Phi < 4$ as shown in Fig. 13. It is also seen in Fig. 13 that our global measurements are qualitatively similar to the local measurements but with a lower peak ratio of about 0.45 compared to 0.6 and with a slight decrease with increasing Φ. The local measurements indicate that the flame chemistry is quenched for $\Phi > 1.5$; Abam [24] has also reported that the methane flame is unreactive for large Φ. It is not surprising that our global measurement of X_{CO}/X_{CO2} is less than the local X_{CO}/X_{CO2}, since some of the CO production locally takes place under fuel lean conditions for which the yield is low.

As mentioned in the Introduction, measurements have been made on the CO and CO_2 concentrations [4,5] versus the global equivalence ratio for turbulent natural gas flames, which were typically 94% methane. In these experiments [4,5] the air entrainment into the flame was controlled by adjusting the height of the collection hood relative to the burner. As shown in Fig. 14, the ratio X_{CO}/X_{CO2} for our study with the laminar methane flame increases much more abruptly with Φ near $\Phi = 1$ compared to the ratio for the turbulent natural gas study [5]. Also, the ratio X_{CO}/X_{CO2} is larger for the laminar burner results for $\Phi > 1$; for example, at $\Phi = 2$, the ratio is 0.46 compared to 0.24 for the turbulent flame.

The effect of Φ on smoke yield is more complex than for CO yield, because not only the yield changes but also the chemical makeup. The decreasing yield of smoke with increasing Φ indicated in Fig. 12 may be a result of the smaller flame height and consequently shorter residence time for smoke particle growth. The much longer reaction time for the formation and growth of smoke particles compared to the formation of CO and CO_2 may also be responsible for the peak in smoke yield occurring at a smaller Φ, which means greater flame height and longer residence time, compared to CO.

As Φ increases, the organic content of the smoke increases and electron microscopy indicates that the smoke agglomerates change from clusters of distinct particles to agglutinated structures with more apparent liquid character. Previous studies [25-27] on the organic content of smoke have been for highly overventilated conditions where the object is burning in the open. Under these conditions for large scale tests, the organic fraction of the smoke was found to be at most 25% for the burning of crude oil, lumber, plywood, heptane, polyurethane, and asphalt shingles. Our results are the first to show that more than 50% of the smoke produced from flaming combustion of a hydrocarbon fuel can be organic. In fact, for methane, 80% to 90% of the smoke is organic for $\Phi = 4$.

It is intriguing to speculate that the high organic content at high equivalence ratio results from the quenching of the smoke growth at an early stage because of the small flame height (Fig. 3). That is, there may be a chemical similarity between this smoke and the incipient smoke in a laminar overventilated diffusion flame. Dobbins *et al.* [27] have reported agglutinated structures of young aggregates when sampling low in a diffusion flame.

Acknowledgements

REFERENCES

1. Burke, S.P. and Schumann, T.E.W. Industrial and Engineering Chemistry 20:998-1004 (1928).

2. Wu, K-T. and Essenhigh, R.H., The Twentieth Symposium (International) on Combustion, The Combustion Institute, 1984, pp. 1925-1932.

3. Sidebotham, G.W. and Glassman, I., Combustion and Flame, 90, pp. 269-283 (1992).

4. Toner, S.J., Zukoski E.E., and Kubota, T., National Bureau of Standards - Grant Contract Research Report 87-528, Gaithersburg, MD (1987)

5. Morehardt, J.H., Zukoski, E.E., and Kubota, T., National Institute of Standards and Technology - Grants Contract Research Report 90-585, Gaithersburg, MD (1990).

6. Beyler, C.L. Fire Safety Journal 10:47-56 (1986).

7. Beyler, C.L. in Proceedings of the First Fire Safety Science International Symposium (C. Grant and P. Pagni, Eds.), Hemisphere, N.Y., 1986, p.431.

8. Roby, R.J. and Beyler, C.L., National Institute of Standards and Technology - Grants Contract Research Report 91-588, Gaithersburg, MD (1991).

9. Bryner, NP, Johnsson, R.L., and Pitts, W.M., National Institute of Standards and Technology - Internal Report, Gaithersburg, MD (1993).

10. Mitchell, R.E., Sarofim, A.F. and Clomburg, L.A. Combustion and Flame 37:227-244 (1980).

11. Smyth, K.C., Miller, J.H., Dorfman, R.C., Mallard, W.G., and Santoro, R.J. Combustion and Flame 62:157-181 (1985).

12. Garo, A., Lahaye, J., and Prado, G. Twenty-First Symposium (International) on Combustion, Combustion Institute, 1023-1031 (1986).

13. Garo, A., Prado, G., and Lahaye, J. Combustion and Flame, 79:226-233 (1990).

14. Kent, J.H. and Wagner, H. Gg. Combustion Science and Technology, 41:245-269 (1984).

15. Santoro, R.J., Semerjian, H.G., and Dobbins, R.A. Combustion and Flame 51:203-218 (1983).

16. Kent, J.H. and Honnery, D.R. Combustion and Flame 82:426-434 (1990).

17. Santoro, R.J., Yeh, T.T., Horvath, J.J., and Semerjian, H.G. Combustion Science and Technology 53:89-115 (1987).

18. Liu, B.Y.H., Pui, D.Y.H., and Rubow,, K.L., in Aerosol in the Mining and Industrial Work Environment, (V.A. Marple and B.Y.H. Liu, Ed.) Elsevier, Amsterdam, 1983, Vol.3, 989.

19. Johnson, R.L., Shah, J.J., Cary,R.A., Huntzicker, J.J.Atmospheric Aerosol:Source/Air Quality Relationships; ACS Symposium Series 167, American Chemical Society, Washington, D.C., 1981.

20. Roper, F.G., Smith, C., and Cunningham, A.C. Combustion and Flame, 29:227-234 (1977).

21. Koylu, K.O., Sivathanu, Y.R., and Faeth, G.M. in Proceedings of the Third Fire Safety Science International Symposium (G. Cox and B. Langford, Eds.), Elsevier, 625-634 (1991).

22. Mulholland, G., Yusa, S., Yanssens, M., Twilley, W., amd Babrauskas, V. in Proceedings of the Third Fire Safety Science International Symposium (G. Cox and B. Langford, Eds.), Elsevier, 585-594 (1991).

23. Puri, R., "The Interaction of Soot Paticles with Carbon Monoxide in Laminar Diffusion Flames", Ph.D. Thesis, The Pennsylvania State University (1992).

24. Abam, D.P.S. Combustion and Flame, 68:95-107 (1987).

25. Mulholland, G.W., Henzel, V., and Babrauskas, V. in Proceedings of the Second Fire Safety Science International Symposium (T. Wakamatsu, Y. Hasemi, A. Sekizawa, P.G. Seeger, P.J. Pagni, and C.E. Grant) 347-357 (1989).

26. Benner, B.A., Bryner, N.P., Wise, S.A., and Mulholland, G.W. Envir. Sci. and Tech., 24:1418-1427 (1990).

27. Dod, R.L., Brown, N.J., Mowrer F.W., Novakov, T., and Williamson, R.B. Aerosol Sci. Tech., 10:20-27 (1989).

28. Dobbins, R.A.and Subramaniasivam, H. Heidleburg Conference entitled "Presentations on Mechanisms and Models of Soot Formation, Heidleburg Conference", October, 1991, to appear in Lecture Notes in Physics, Springer-Verlag.

FIGURES

1. Illustration of burner, dilution system, and probe assembly.

2. Illustration of sampling and analysis system.

3. Flame photographs of methane at a fuel flow of 10 cm^3/s and ethene at fuel flow of 6.4 cm^3/s versus Φ for burner configuration 1.

4. Volume % of CO and CO_2 versus logΦ for a methane flame with fuel flow of 10 cm^3/s (data from Table 2).

5. Yield of CO for methane at a flow of 10 cm^3/s (Δ) and for ethene at a flow of 6.4 cm^3/s (O) versus Φ based on data in Table 2 and repeat measurements made on another day.

6. Yield of CO for ethene at a flow of 6.4 cm^3/s (O) and a flow of 3.2 cm^3/s (∇) versus Φ.

7. Yields of CO (O) and smoke ($\bullet$) as function of Φ for ethene at a flow of 6.4 cm^3/s.

8.   Yield of smoke for ethene at a flow of 6.4 cm^3/s (●) and for methane at a flow of 10 cm^3/s (▲).

9.   Yield of smoke for ethene at a flow of 6.4 cm^3/s (●) and at a flow of 3.2 cm^3/s (▼).

10. Yield of CO (burner config. 1, ○; burner config. 2,▽) and smoke (burner config. 1, ●; burner config. 2, ▼) for ethene at 6.4 cm^3/s.

11. TEM photographs of smoke collected from an ethene flame at $\Phi = 1$ (left) and at $\Phi = 4$ (right).

12. Yield of CO (○) and smoke (●) per g of oxygen consumed for ethene at a flow of 6.4 cm^3/s.

13. Local ratio X_{CO}/X_{CO2} versus local equivalence ratio for overventilated methane flame (●), for underventilated methane flame (▲), and global ratio X_{CO}/X_{CO2} versus global equivalence ratio for underventilated methane flame (Δ, this study).

14. X_{CO}/X_{CO2} versus Φ for laminar burning of methane at a flow of 10 cm^3/s (Δ) and for turbulent burning of natural gas (♦).

TABLES

1.   Tube dimensions for coflow burners.

2.   Results for burner configuration 1 for the methane and ethene flames.

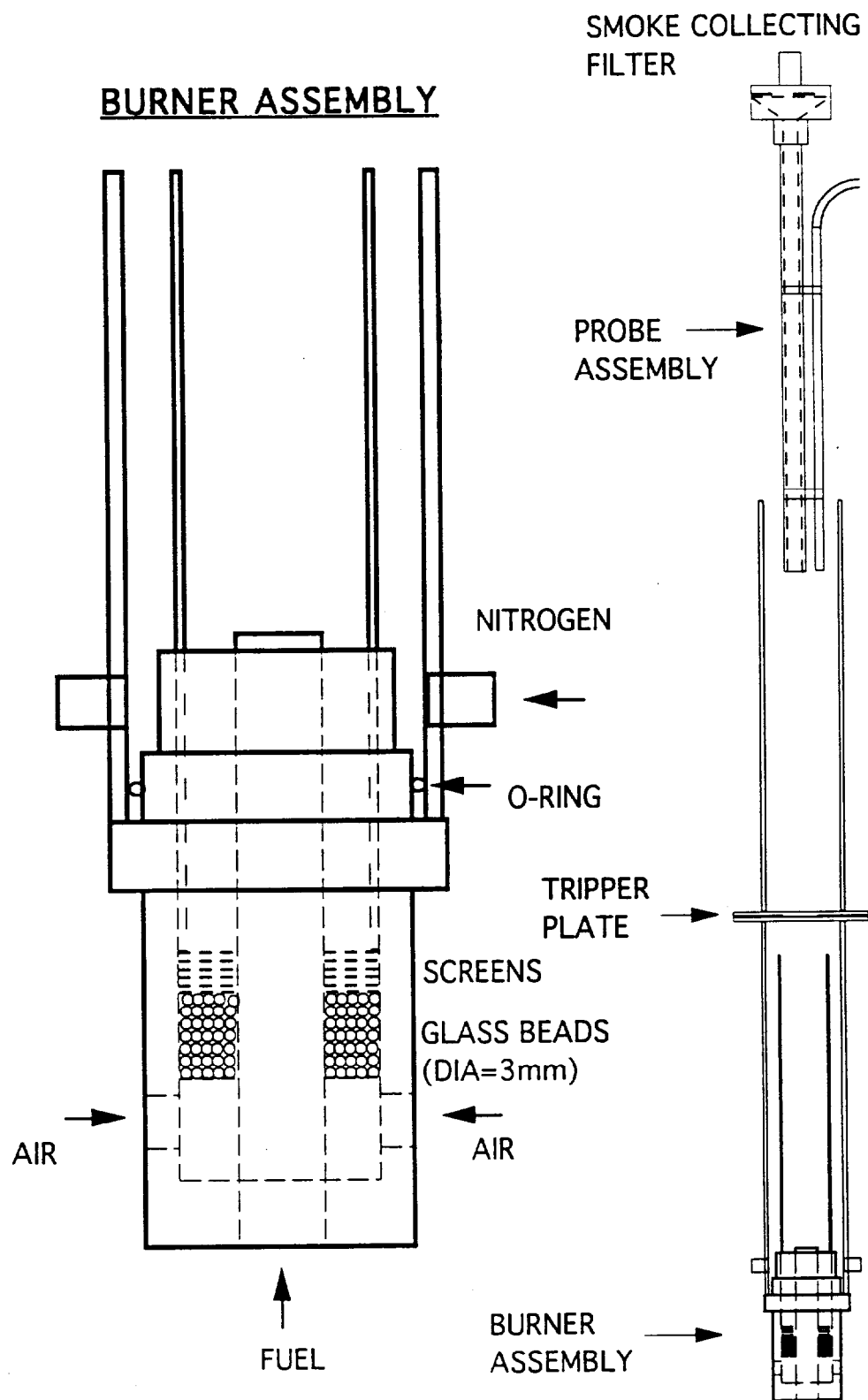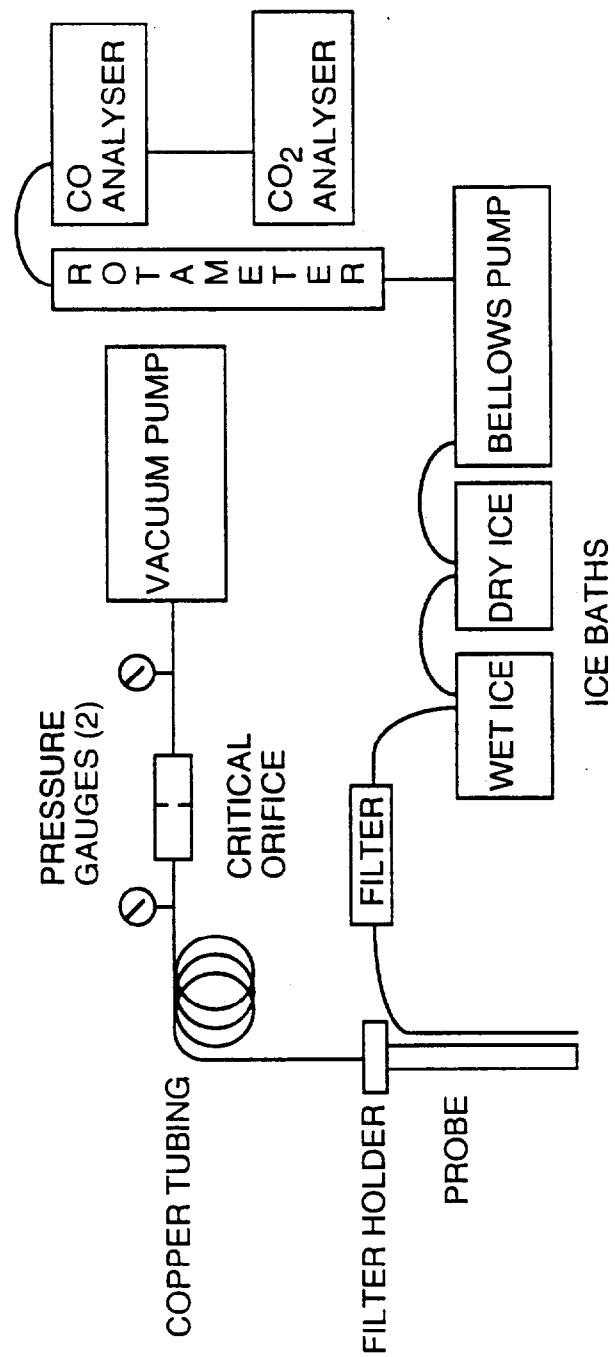3.   Organic and elemental carbon analysis of smoke.

BURNER ASSEMBLY

SMOKE COLLECTING
FILTER

PROBE
ASSEMBLY

NITROGEN

O-RING

SCREENS

GLASS BEADS
(DIA=3mm)

AIR

AIR

TRIPPER
PLATE

FUEL

BURNER
ASSEMBLY

Figure 1

CO ANALYSER

CO_2 ANALYSER

ROTAMETER

VACUUM PUMP

BELLOWS PUMP

PRESSURE GAUGES (2)

CRITICAL ORIFICE

DRY ICE

WET ICE

ICE BATHS

FILTER

COPPER TUBING

FILTER HOLDER

PROBE

Figure 2

Laminar Diffusion Flames

—— Predicted Flame Height   (All Dimensions in mm)

Methane 10 cm³/s
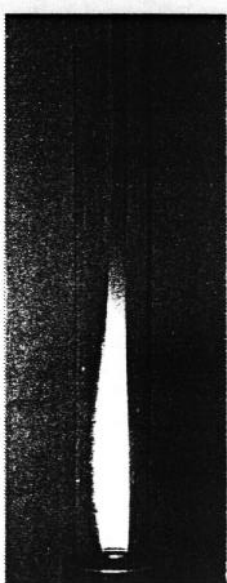
Φ = 1.0   Φ = 1.5   Φ = 2.5   Φ = 4.0

48   19   9

Ethene 6.4 cm³/s
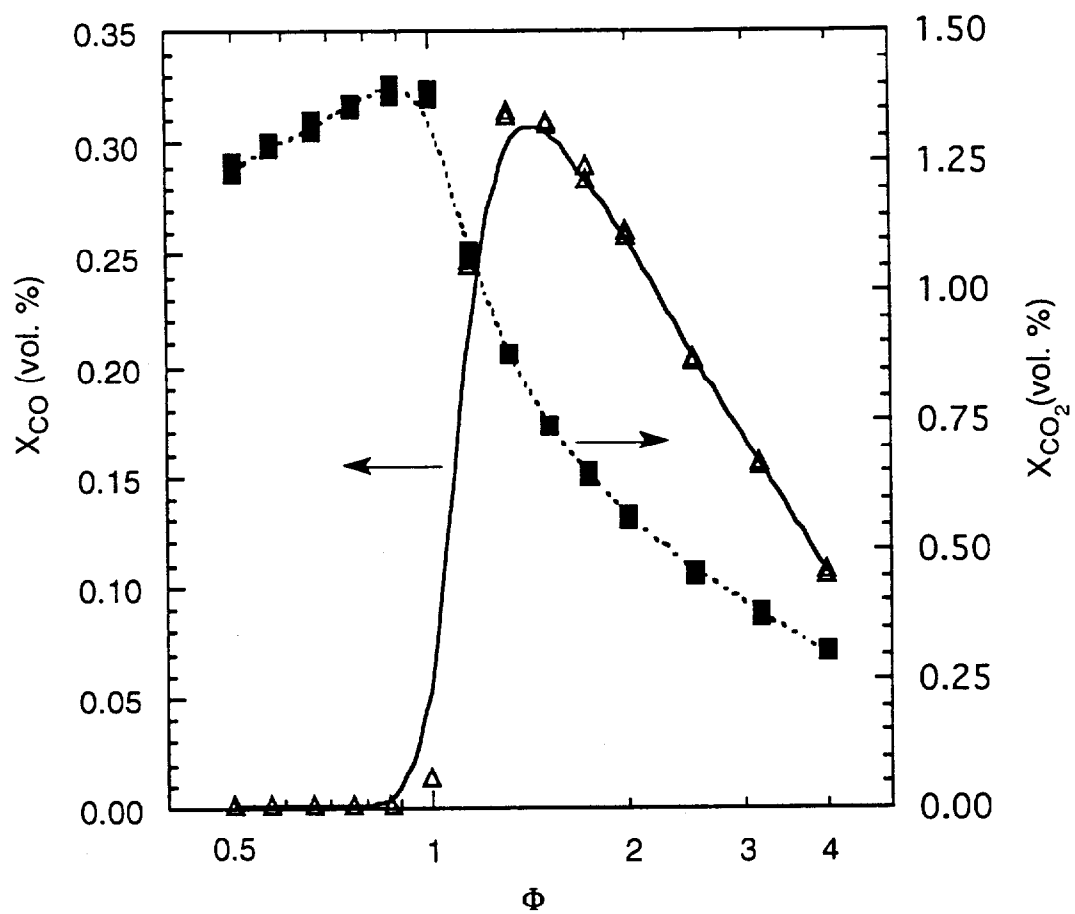
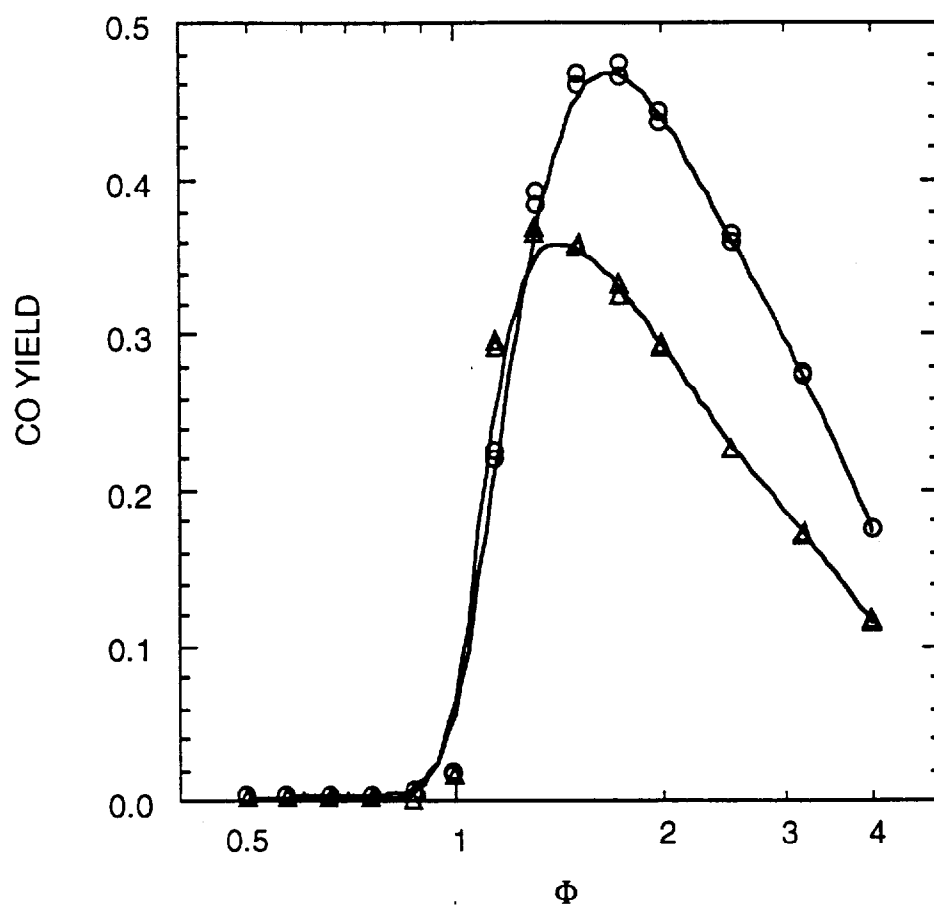Φ = 1.0   Φ = 1.5   Φ = 2.5   Φ = 4.0
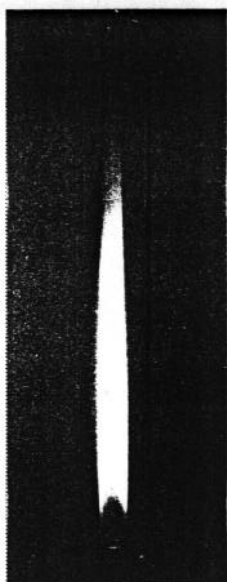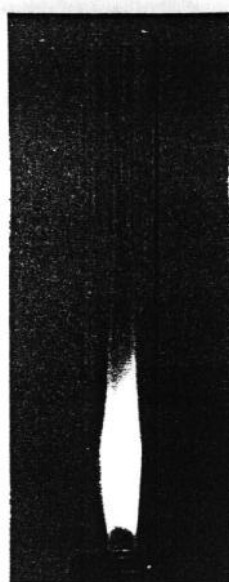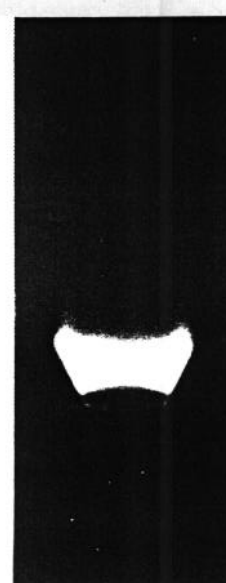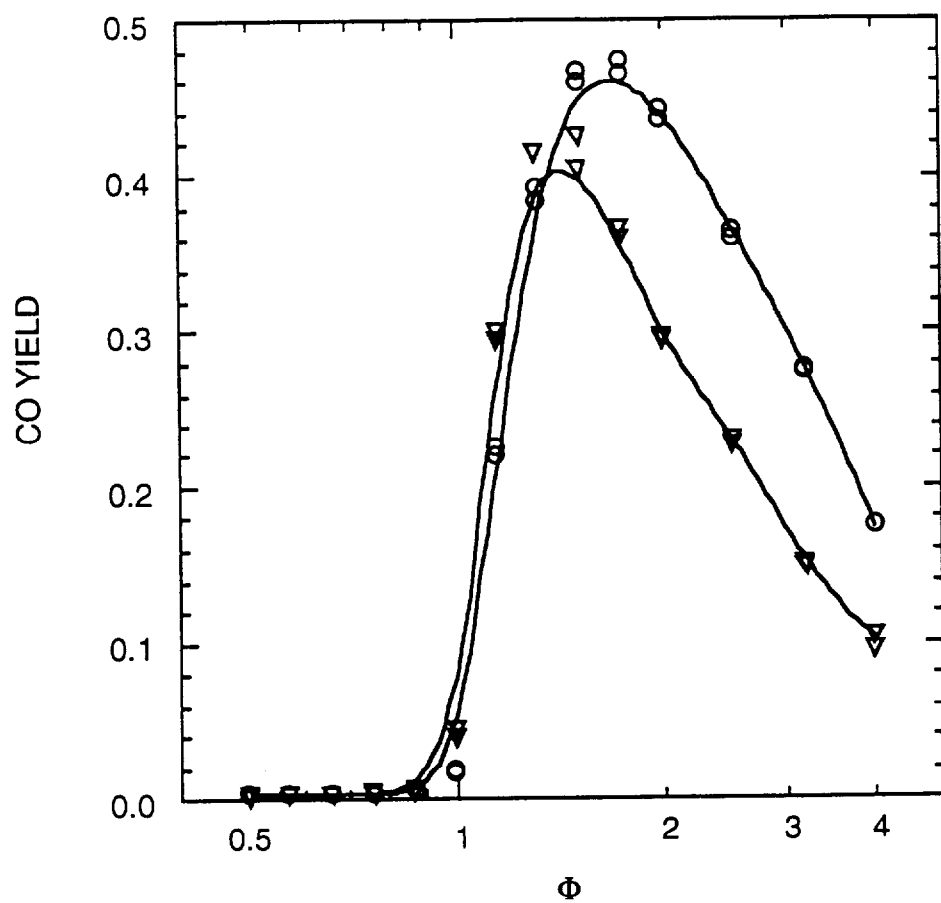
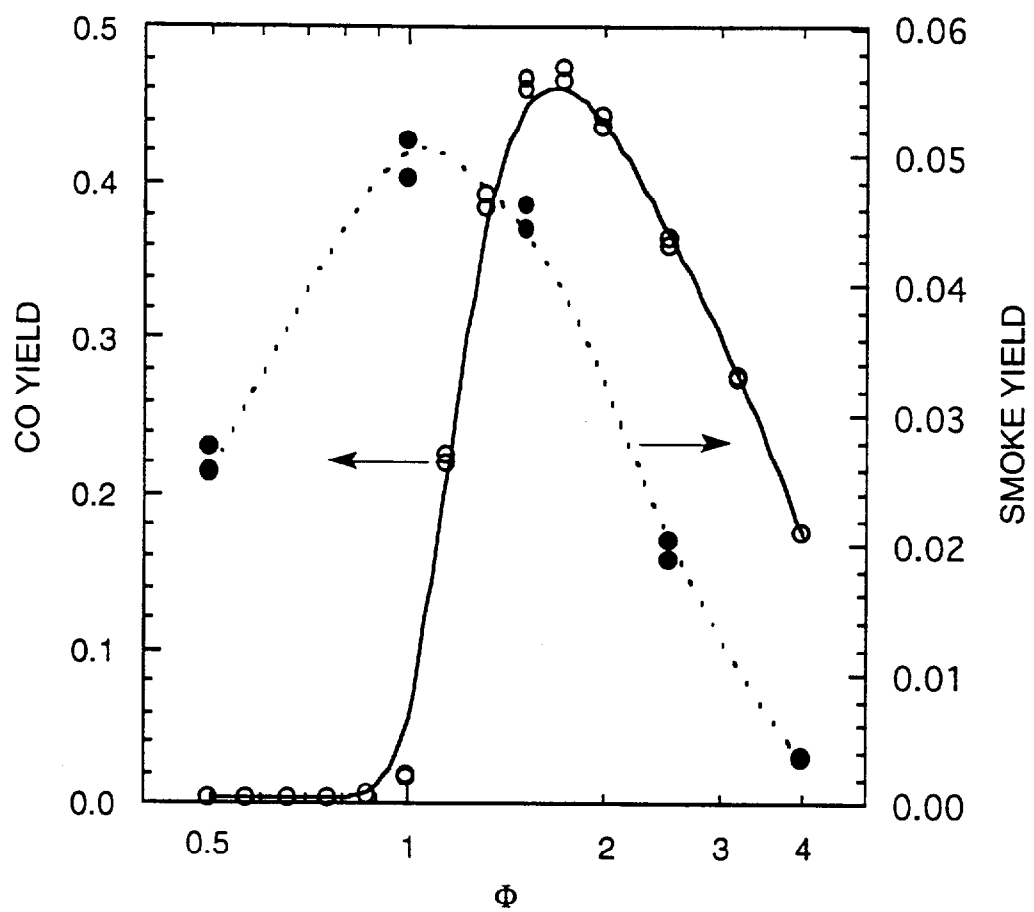

45   18   8

Figure 4

Figure 5

Figure 6

Figure 7
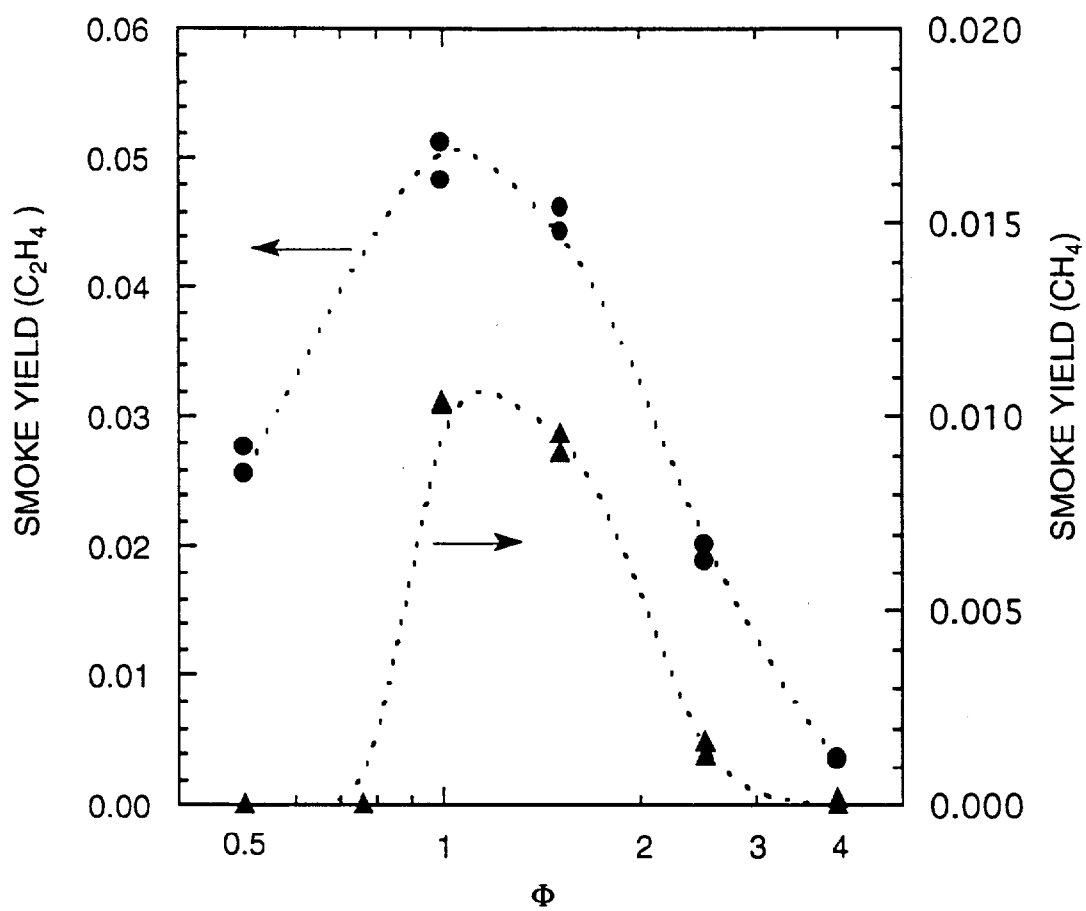
Figure 8
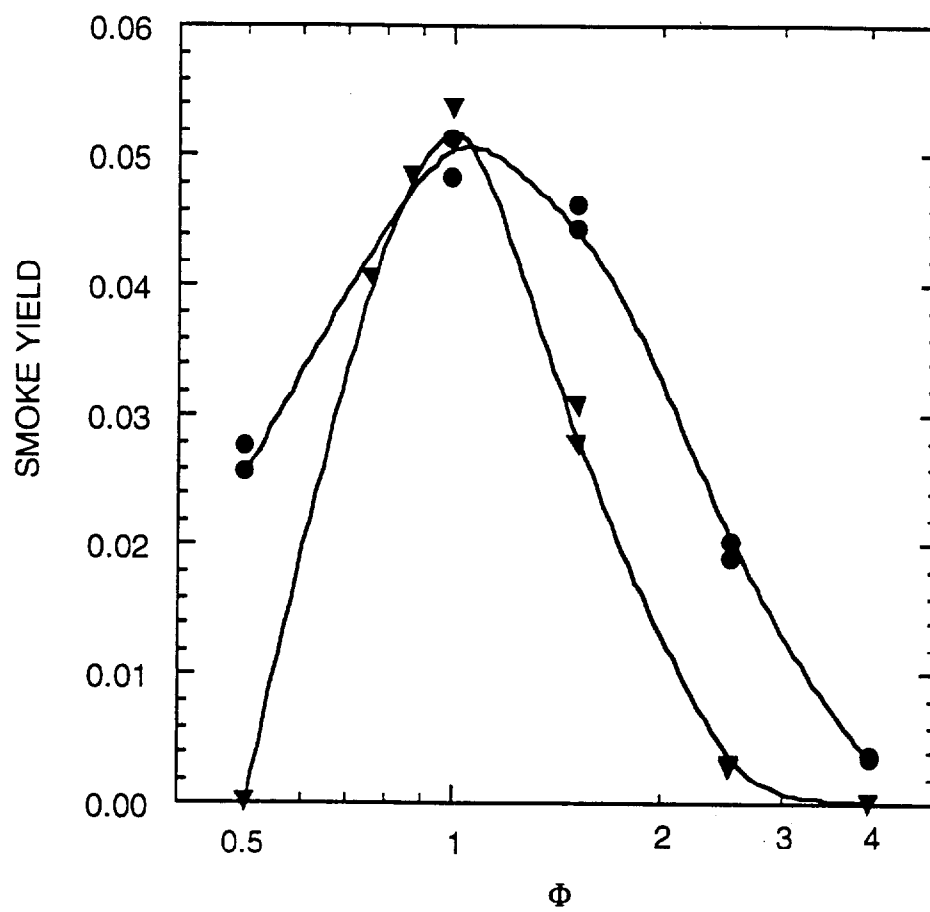
Figure 7
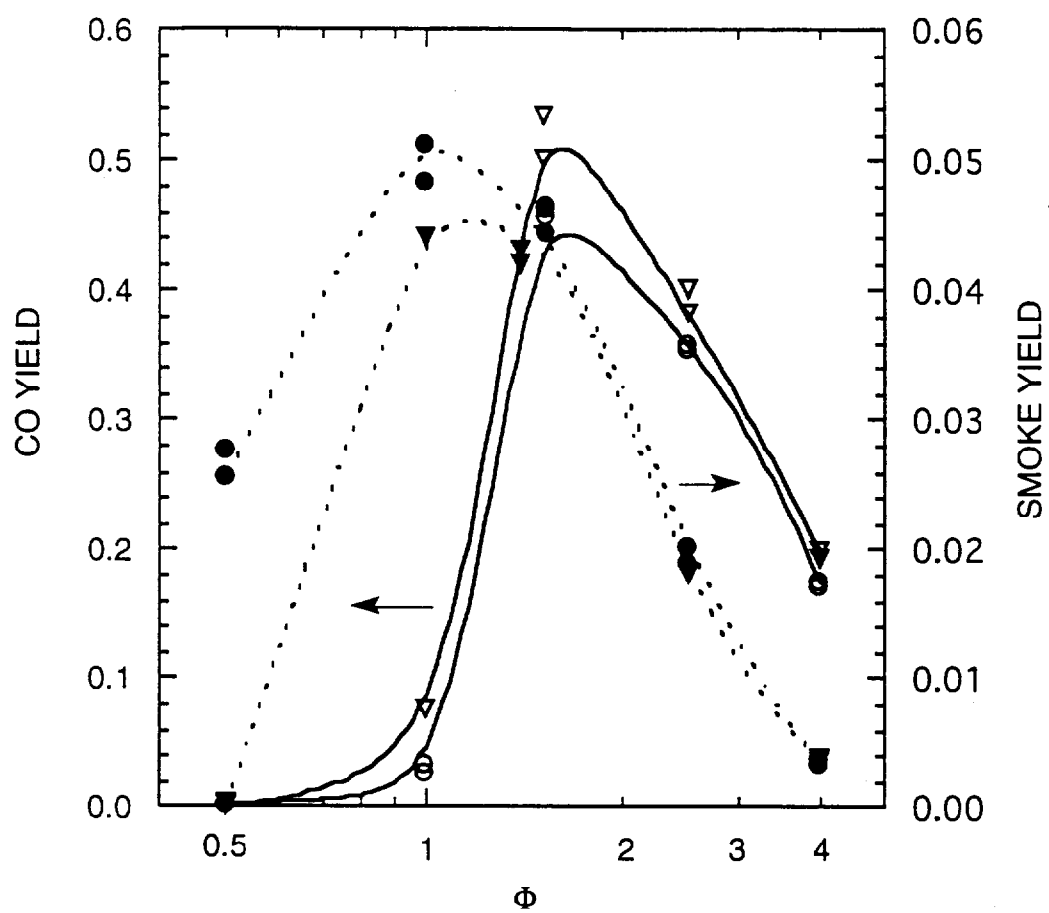
Figure 10

Smoke collected from an Ethene flame.

$\Phi = 1.0$

$\Phi = 4.0$

0.5 μm
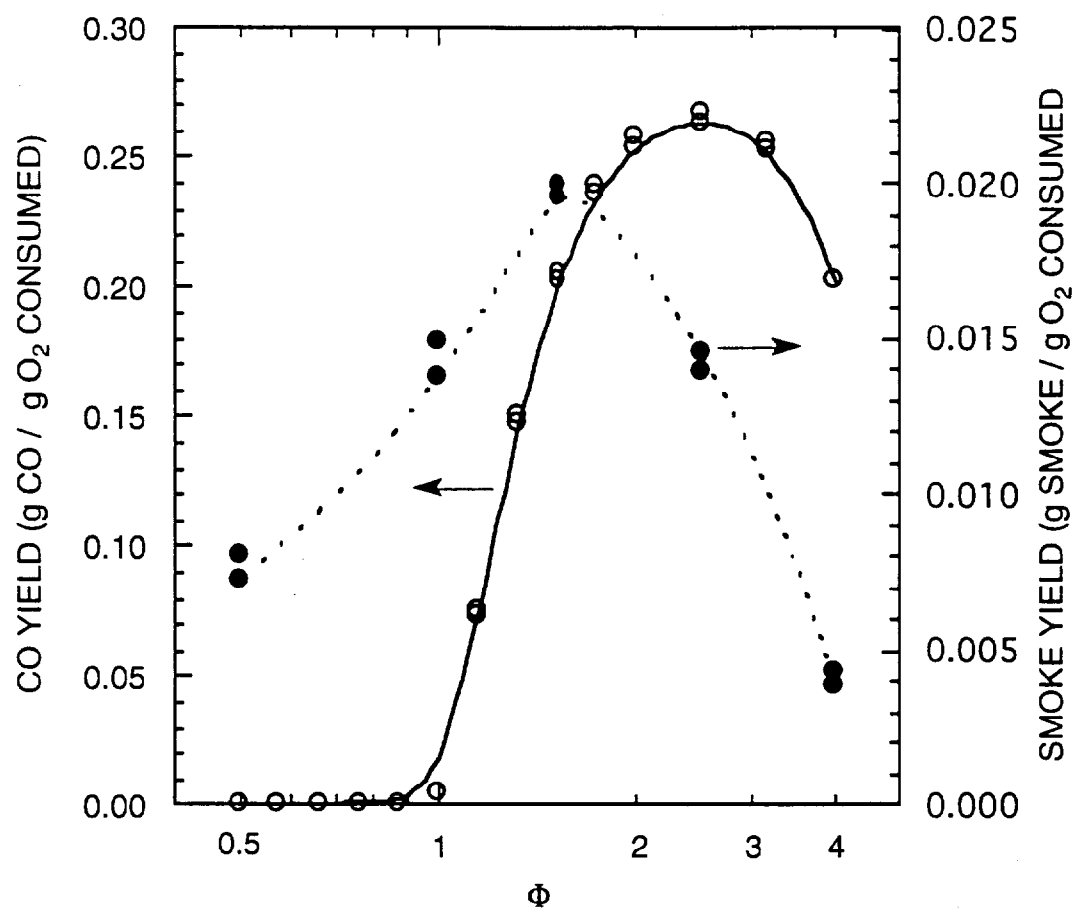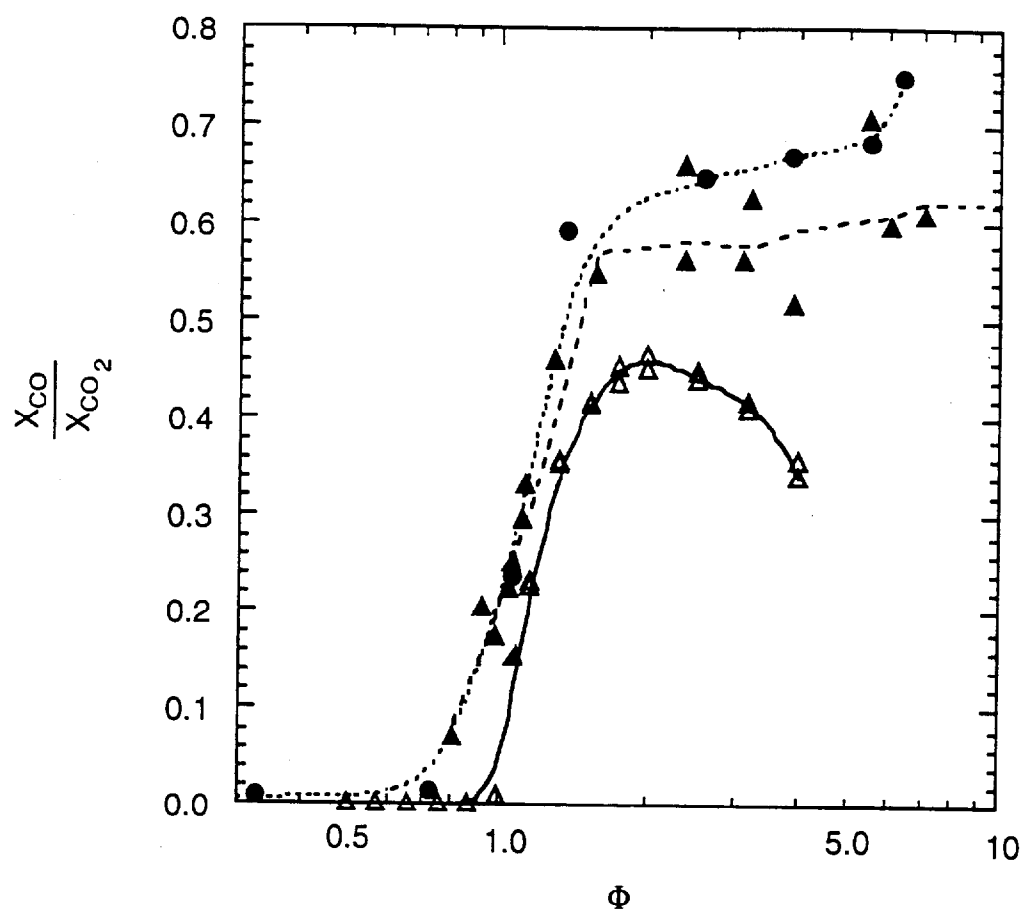
Figure 11

Figure 12

Figure 13
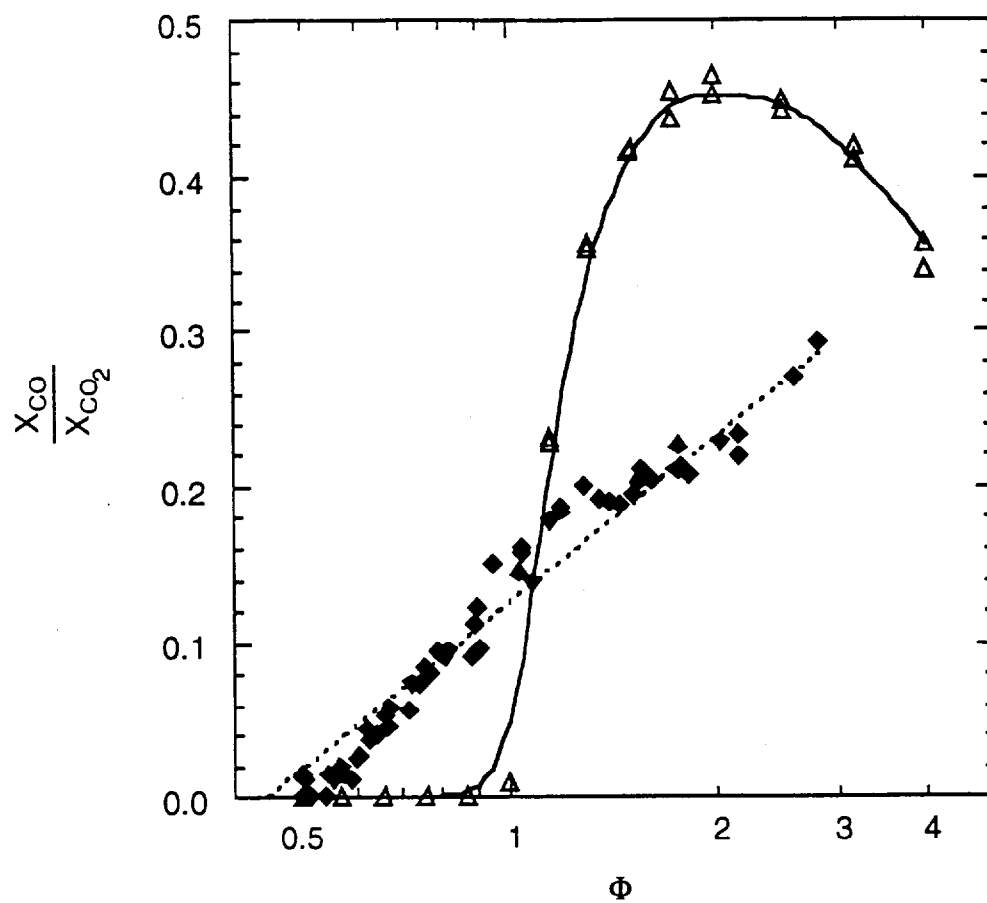
Figure 14

Table 1

Tube Dimensions for Coflow Burners

	Inner Tube (mm) [1]	Outer Tube (mm) [2]
Burner Configuration 1	9.6 O.D. (⅜") 7.3 I.D.	29 I.D. 32 O.D. (28×32)[3]
Burner Configuration 2	9.6 O.D. (⅜") 7.3 I.D.	22 I.D. 25 O.D. (22×25)[3]
Burner Configuration 3	12.7 O.D. (½") 11.2 I.D.	22 I.D. 25 O.D. (22×25)[3]

[1] Brass

[2] Quartz

[3] Nominal size for ordering

Table 2.
Results for Burner Configuration 1 for Methane and Ethene

Methane 10 cm³/s Dilution 590 cm³/s of N₂ (06/17/92)

Φ	air flow cm³/s	total flow cm³/s	X_{CO} vol. %	X_{CO2} vol. %	smoke mg	ε_{CO} gCO/gCH4	ε_{CO2} gCO2/gCH4	ε_s gC/gCH4	carbon balance
0.50	190	790	0.001	1.25		0.001	2.72		0.99
0.57	166	766	0.001	1.29		0.001	2.72		0.99
0.66	144	744	0.001	1.33		0.001	2.72		0.99
0.76	126	726	0.001	1.36		0.001	2.71		0.99
0.87	109	709	0.001	1.40		0.001	2.73		0.99
1.00	95.2	695	0.013	1.39		0.016	2.66		0.97
1.15	82.8	683	0.245	1.08		0.293	2.03		0.90
1.32	72.2	672	0.311	0.88		0.366	1.63		0.80
1.52	62.8	663	0.308	0.74		0.357	1.35		0.69
1.74	54.7	655	0.284	0.65		0.325	1.17		0.61
2.00	47.7	648	0.258	0.57		0.292	1.02		0.54
2.52	37.8	638	0.203	0.46		0.227	0.81		0.42
3.18	30.0	630	0.156	0.38		0.172	0.66		0.34
4.00	23.8	624	0.105	0.31		0.115	0.53		0.26

Methane 10 cm³/s Dilution 590 cm³/s of N₂ (04/11/92)
T = 23°C, P = 731.7 mmHg, Sampling 152 cm³/s

Φ	air flow cm³/s	total flow cm³/s	X_{CO} vol. %	X_{CO2} vol. %	smoke mg	ε_{CO} gCO/gCH4	ε_{CO2} gCO2/gCH4	ε_s gC/gCH4	carbon balance
0.50	190	790	0.0	1.23	0.0	0.0	2.67	0.0	0.97
1.00	95.2	695	0.055	1.31	4.29	0.067	2.50	0.010	0.96
1.52	62.8	663	0.305	0.72	4.68	0.354	1.31	0.009	0.69
2.52	37.8	638	0.205	0.44	0.79	0.229	0.77	0.0013	0.41
4.00	23.8	624	0.102	0.29	0.0	0.111	0.50	0.0	0.24

Ethene 6.4 cm³/s Dilution 590 cm³/s of N₂ (06/17/92)

Φ	air flow cm³/s	total flow cm³/s	X_{CO} vol. %	X_{CO2} vol. %	smoke mg	ε_{CO} gCO/gC₂H₄	ε_{CO2} gCO₂/gC₂H₄	ε_s gC/gC₂H₄	carbon balance
0.50	183	779	0.002	1.52		0.002	2.91		0.93
0.57	159	755	0.002	1.57		0.002	2.91		0.93
0.66	139	735	0.002	1.60		0.002	2.89		0.92
0.76	121	717	0.003	1.63		0.003	2.87		0.91
0.87	105	701	0.005	1.65		0.006	2.84		0.91
1.00	91.3	688	0.015	1.66		0.016	2.80		0.90
1.15	79.5	676	0.209	1.42		0.221	2.36		0.86
1.32	69.2	666	0.369	1.16		0.384	1.90		0.79
1.52	60.3	657	0.448	0.95		0.459	1.53		0.72
1.74	52.5	649	0.459	0.80		0.465	1.27		0.64
2.00	45.7	642	0.434	0.68		0.435	1.07		0.56
2.52	36.3	633	0.363	0.53		0.359	0.82		0.44
3.18	28.8	625	0.280	0.44		0.273	0.68		0.35
4.00	22.8	619	0.180	0.35		0.174	0.53		0.26

Ethene 6.4 cm³/s Dilution 590 cm³/s of N₂ (04/23/92)
T = 23°C, P = 736.4 mmHg, Sampling 155 cm³/s

Φ	air flow cm³/s	total flow cm³/s	X_{CO} vol. %	X_{CO2} vol. %	smoke mg	ε_{CO} gCO/gC₂H₄	ε_{CO2} gCO₂/gC₂H₄	ε_s gC/gC₂H₄	carbon balance
0.50	183	779	0.002	1.51	7.03	0.002	2.89	0.028	0.94
1.00	91.3	688	0.032	1.60	14.70	0.034	2.70	0.051	0.91
1.52	60.3	657	0.446	0.93	13.70	0.457	1.50	0.044	0.73
2.52	36.3	633	0.358	0.51	5.95	0.354	0.79	0.019	0.44
4.00	22.8	619	0.177	0.33	1.99	0.171	0.50	0.0037	0.25

Table 3.

Organic and Elemental Carbon Analysis

Methane 10 cm³/s

Φ	Organic Carbon µg/cm²	Organic Carbon Error	Elemental Carbon µg/cm²	Elemental Carbon Error	Organic/Elemental
1	1.0	0.2	21	1	0.05
2	8.4	0.5	4.9	0.3	1.7
4	3.4	0.3	0.4	0.1	8.5
4	5.2	0.4	1.0	0.2	5.2

Ethene 6.4 cm³/s

Φ	Organic Carbon µg/cm²	Organic Carbon Error	Elemental Carbon µg/cm²	Elemental Carbon Error	Organic/Elemental
0.50	0.7	0.1	19	1	0.04
1	1.3	0.2	27	1	0.05
2	7.2	0.5	15	0.9	0.48
4	7.0	0.5	6.2	0.4	1.13